

1 **Bioresorbable, miniaturized porous silicon needles on flexible water-  
2 soluble backing for unobtrusive, sustained delivery of chemotherapy**

3  
4 *Hyungjun Kim<sup>†,‡,§</sup>, Heungssoo Lee<sup>§,‡</sup>, Yale Jeon<sup>§</sup>, Woohyun Park<sup>¥</sup>, Yue Zhang<sup>||</sup>, Bongjoong Kim<sup>¥</sup>,  
5 Hanmin Jang<sup>§</sup>, Baoxing Xu<sup>||</sup>, Yoon Yeo<sup>‡,\*</sup>, Dong Rip Kim<sup>§,\*</sup>, Chi Hwan Lee<sup>†,¥,‡,§,\*</sup>*

6  
7 <sup>†</sup>Weldon School of Biomedical Engineering, Purdue University, West Lafayette, IN 47907, USA.

8 <sup>‡</sup>Department of Industrial and Physical Pharmacy, Purdue University, West Lafayette, IN 47907,  
9 USA.

10 <sup>§</sup>School of Mechanical Engineering, Hanyang University, Seoul, South Korea.

11 <sup>¥</sup>School of Mechanical Engineering, Purdue University, West Lafayette, IN 47907, USA.

12 <sup>||</sup>Department of Mechanical and Aerospace Engineering, University of Virginia, Charlottesville,  
13 VA 22904, USA

14 <sup>‡</sup>School of Materials Engineering, Purdue University, West Lafayette, IN 47907, USA.

15 <sup>§</sup>Department of Speech, Language, and Hearing Sciences, Purdue University, West Lafayette, IN  
16 47907, USA

17  
18 **ABSTRACT:** Conventional melanoma therapies suffer from the toxicity and side effects of  
19 repeated treatments due to the aggressive and recurrent nature of melanoma cells. Less-  
20 invasive topical chemotherapies by utilizing polymeric microneedles have emerged as an  
21 alternative, but the sustained, long-lasting release of drug cargos remains challenged. In  
22 addition, the size of the microneedles is relatively bulky for the small, curvilinear, and  
23 exceptionally-sensitive cornea for the treatment of ocular melanoma. Here, we report a  
24 design of bioresorbable, miniaturized porous-silicon (p-Si) needles with covalently-linked  
25 drug cargos at doses comparable to those of conventional polymeric microneedles. Uniquely,  
26 the p-Si needles are built on a water-soluble film as a temporary flexible holder that can be  
27 intimately interfaced with the irregular surface of living tissues, followed by complete  
28 dissolution with saline solution within one minute. Consequently, the p-Si needles remain  
29 embedded inside tissues and then undergo gradual degradation allowing for sustained  
30 release of the drug cargos. Its utility in unobtrusive topical delivery of chemotherapy with  
31 minimal side effects is demonstrated in a murine melanoma model.

32  
33 Keywords: *Melanoma Treatment, Topical Drug Delivery, Bioresorbable Silicon Nanomaterials,  
34 Sustained Drug Release*

Melanoma – the most serious form of skin cancer – is typically caused by ultraviolet radiation from natural sunshine or tanning beds and developed at the stratum corneum of epidermis (15-25  $\mu\text{m}$  from the skin surface).<sup>1</sup> Given the aggressive and recurrent nature of melanoma cells, repeated treatments are often necessary, thereby increasing the risk of toxicity and side effects.<sup>2</sup> An effective treatment involves using the topical administration of chemotherapeutics into tumor tissues using polymeric microneedles as a less-invasive and painless route.<sup>3,4</sup> Recently, further miniaturized nanoscale needles made of porous-silicon (p-Si) emerge as an attractive candidate for intratissue injection that can offer favorable safety profile and controlled biodegradability.<sup>5-7</sup> Compared to conventional polymeric microneedles, the miniaturized p-Si needles benefit from their amenability to existing nanofabrication processing, and therefore provide the following key advantages: (1) precise control of the size, geometry, tapering, and tip morphology at the nanoscale,<sup>8</sup> (2) rational tuning of porosity on the surface (in turn, drug loading capacity),<sup>6,9</sup> (3) pre-programmable dissolution rate of the p-Si needles through surface oxidations (encapsulation),<sup>10,11</sup> (4) uniform delivery owing to the high density of the p-Si needles per projected surface area,<sup>5</sup> and (5) long-lasting release of covalently-linked drug cargos by gradual degradation of the p-Si needles in tissue fluids over time.<sup>9,12</sup> These attributes are important for controlled, sustained, and minimally-invasive topical delivery of therapeutics.

However, challenges still remain in that the vertically-ordered arrays of the p-Si needles are built on a rigid Si wafer that can accommodate the conditions required for conventional nanofabrication processing such as thermal annealing, corrosive chemical etching, and photolithographic patterning.<sup>13</sup> The use of the rigid Si wafer results in a mechanical mismatch when interfaced with the soft, curvilinear, and dynamic surface of living tissues. This discordance leads to debasing of the interfacial contact quality, which is particularly problematic in their application to the small, curvilinear, and exceptionally-sensitive cornea where melanoma is occasionally formed (i.e., ocular melanomas).<sup>14</sup> Our recent work demonstrated that these challenges can be alleviated to some extent by building the miniaturized p-Si needles on a thin, flexible backing film made of silicone elastomer such as polydimethylsiloxane (PDMS) for their use in intracellular drug delivery.<sup>15</sup> A disadvantage of this construct is that the flexible PDMS backing film may cause irritation or discomfort to the wearer especially under vigorous deformations of tissues by body movements. Complete elimination of the backing film after the insertion of the p-Si needles into tissues may resolve the physical strains, thereby enabling unobtrusive topical delivery of therapeutics over a prolonged period of time.

Here, we introduce a bioresorbable, miniaturized p-Si needles loaded with covalently-linked drug cargos, which is built on a thin, flexible, and water-soluble film. The water-soluble film is temporarily used during the insertion of the p-Si needles into tissues, and then can be immediately dissolved within one minute by the application of saline solution. Consequently, the p-Si needles remain embedded inside tissues and, due to the nanoscale size, become unobtrusive (nearly unnoticeable) to the wearers without affecting their natural motions. The p-Si needles subsequently undergo gradual hydrolysis in tissue fluids to degrade into biocompatible byproducts, leading to sustained, long-lasting release of preloaded drug cargos over days at a controlled rate. Comprehensive experimental and computational studies provide an insight into the structural design and construction of the p-Si needles on a water-soluble backing over centimeter-scale areas and elucidate the fundamental attributes. Comprehensive demonstrations of the p-Si needles for the topical delivery of chemotherapy in a murine melanoma model illustrate the utility of this concept.

## RESULTS AND DISCUSSION

**Design principle and fabrication process.** Figure 1A schematically illustrates the basic procedure to integrate the bioresorbable, miniaturized p-Si needles with a thin, flexible, and water-soluble medical film such as polyvinyl alcohol (PVA; medical-grade; mechanical modulus ( $E$ ) = 3.4 GPa; molecular weight of ~31,000; Sigma Aldrich, USA). The first step is to fabricate an array of vertically-ordered p-Si needles on a polished monocrystalline Si wafer through sequential steps of photolithographic patterning, dry and wet etchings, and metal-assisted chemical etching (MACE) (Figure 1A, left).<sup>15</sup> This step also formed uniform undercuts and nanopores at the bottom and on the surface of the p-Si needles, respectively (inset image). Details of the fabrication procedures are shown in the Materials and Methods section. Figure S1 shows representative scanning electron microscopy (SEM) images of the as-fabricated p-Si needles, exhibiting the minimum tip diameter ( $d$ ) of 150 nm, the base diameter ( $D$ ) of 2-4  $\mu$ m, and the length ( $L$ ) of 10-70  $\mu$ m. In the next step, the entire structure was spin-cast with a 10 weight % PVA (200-300  $\mu$ m-thick), allowing an air gap to form at the interface due to surface tension (Figure 1A, middle). The length of the p-Si needles was determined by this air gap that was adjusted by controlling the spin-casting speed within the range from 300 rpm to 500 rpm, leading to the consequent air gap size of ~20  $\mu$ m and ~50  $\mu$ m, respectively (Figure S2). The spin-casting of the PVA film was repeated until its total thickness reached about 200-300  $\mu$ m to provide sufficient mechanical strength for handling. Subsequently, a thermal annealing was followed to complete the solidification of the PVA film using a convection oven maintained at 70 °C for 30 min. Finally, the fully cured PVA film was peeled from the Si wafer at constant peeling rate of 50 mm/min using an automated peeling apparatus (Mark-10, Willrich Precision Instrument) (Figure 1A, right). During this peeling process, mechanical stress can be concentrated predominantly at the bottom undercuts of the p-Si needles to generate cracks allowing for their physical liberation from the Si wafer.<sup>15</sup>

Figure 1B shows representative photograph (left) and enlarged microscope image (right) of the physically-transferred p-Si needles to a thin layer (200–300  $\mu$ m-thick) of a PVA film. The intrinsically thin and flexible property of the PVA film can facilitate intimate contact to the soft, irregular surface of tissues, while the sharpened angular tip of the p-Si needles facilitates easier penetration.<sup>15,16</sup> The overall height, vertical arrangement, and tip morphology of the transferred p-Si needles were consistent across the entire specimen area ( $3 \times 3$  cm $^2$ ). Figure S3 shows the fractured planes on both the donor Si wafer and the receiver PVA film, suggesting that the cracking occurred uniformly at the bottom undercut of the p-Si needles. Figure 1C shows the nanopores formed on the surface of the p-Si needles in which the porosity (in turn, drug loading capacity) can be adjusted during the MACE process. The SEM images in Figure S4 provide representative examples of the p-Si needles configured into different surface porosities (0%, ~30%, ~45%, and ~60%) that were controlled by the MACE time of 0, 30, 60, and 90 s, respectively. Figure S5 presents a series of optical images at various stages during the dissolution of the PVA film - colored with yellow food dye (McCormick & Company, USA) for visualization - when immersed in 50 ml of phosphate-buffered saline (PBS; pH 7.4; Sigma-Aldrich, USA) at 37.5 °C. The complete dissolution of the PVA film occurred typically within 10-15 min in this condition (Movie S1, Supporting Information), or it can be swabbed away using a saline-moistened cotton swab in less than 1 min.

The controlled cracking at the bottom undercut of the p-Si needles over centimeter-scale areas is crucial to successful implementation of this approach. Figure S6 shows an experimental setup and the corresponding experimental results for peeling load–peeling distance curve for a specimen ( $3 \times 3$  cm $^2$ ,  $d$  = 1  $\mu$ m,  $D$  = 4  $\mu$ m, and  $L$  = 50  $\mu$ m) under constant peeling of the PVA film at 50

1 mm/min. Movie S2 (Supporting Information) demonstrates the real-time measurement process.  
2 The results indicate that the peeling load increased rapidly to a maximum and initiate cracking,  
3 and then reached a plateau for steady-state crack propagation. Figure 1D shows finite element  
4 analysis (FEA) results, revealing that the principal strain ( $\epsilon$ ) remained localized near the bottom  
5 undercut of the p-Si needles during the constant peeling. The tendency for the localization of  $\epsilon$  was  
6 more evident as the D/d ratio was increased, wherein the peak principal strain ( $\epsilon_{peak}$ ) was larger  
7 than the fracture limit (~1%) of the p-Si needles when D/d > 1.5 (Figure S7). The experimental  
8 and FEA results of strain energy release rate (G) for the cracking are summarized in Figure 1E.  
9 The green-filled area denotes where the cracking typically occurred with high-fidelity. Figure 1F  
10 experimentally and theoretically reveals the dependence of G on peeling rate ( $v$ ) of the PVA film.  
11 The results showed a clear power-law relationship of them (i.e., the G increased rapidly at low  $v$   
12 and then gradually reached steady-state) due to the viscoelastic property of the PVA film.<sup>17</sup> For  
13 instance, a rapid peeling ( $v > 20$  mm/min) of the PVA film provided sufficiently large adhesive  
14 strength to peel the p-Si needles away from the Si wafer. On the other hand, a slow peeling ( $v <$   
15 20 mm/min) of the PVA film was unable to hold the p-Si needles, resulting in compressed marks  
16 left on the surface (Figure S8). For the theoretical analysis, the energy release rate was obtained  
17 by assuming that the PVA film was monolithically bonded to the p-Si needles without embedding  
18 inside, causing the discrepancy with the experimental results especially at high peeling rate ( $v >$   
19 100 mm/min).

20  
21 **Controlled dissolution of the p-Si needles in biological fluids.** Figure 2A show the gradual  
22 dissolution of a unit array ( $1 \times 1$  cm $^2$ ) of the p-Si needles with fixed initial base diameter ( $D_0$ ) of 3  
23  $\mu\text{m}$  when immersed in 50 ml of PBS (pH 7.4) at 37.5 °C for 90 days, while refreshing the solution  
24 every 10 days to maintain the pH value. The magnified SEM images of the p-Si needles at  
25 predetermined time interval are shown in Figure S9. The dissolution of the p-Si needles occurred  
26 via hydrolysis of Si to silicic acid and hydrogen (i.e.,  $\text{Si} + 4\text{H}_2\text{O} \leftrightarrow \text{Si}(\text{OH})_4 + 2\text{H}_2$ ), which involves  
27 nucleophilic attack at the surface to weaken the interior bonds of Si atoms.<sup>18-20</sup> The dissolution  
28 kinetics rely on the pH, temperature, and ionic strength of the solution as well as the pre-defined  
29 surface porosity of Si.<sup>10</sup> Figure 2B shows measurement results of the gradual diameter reduction  
30 ( $D/D_0$ ) of the p-Si needles with varied surface porosities, indicating that the dissolution rate was  
31 increased from ~10 nm/day to ~20 nm/day as the surface porosity was increased from 0% to 60%.  
32 Figure 2C and D compare the dissolution of the p-Si needles in higher pH environment (PBS; pH  
33 10.0) at 37.5 °C. The results indicate that the dissolution rate was substantially accelerated at  
34 higher pH, while the rate was non-linearly decreased over time due to enhanced dependence on  
35 the concentration of the byproducts, such as  $\text{Si}(\text{OH})_4$ , in the solution.<sup>19</sup> In fact, the biosafety of the  
36 monocrystalline Si nanomaterials and their dissolution products has been proved in many  
37 biomedical applications, without showing measurable cytotoxic effects.<sup>10,11,19</sup>

38 Figure 2E shows a series of snapshot images obtained from molecular dynamics (MD)  
39 simulation at different time frames, revealing the dissociation process of a Si atom (highlighted in  
40 blue) in water ( $\text{H}_2\text{O}$ ) due to the effect of nucleophile attack by OH- groups (enlarged). At the  
41 beginning ( $t = 0.5$  ns), no bonding occurred between the Si atom and OH- groups. At  $t = 3$  ns, an  
42 OH- group started attacking the Si atom to create a bond. At  $t = 4$  ns, another OH- group attacked  
43 the Si atom and formed another bond to break an interior Si-Si bond. At  $t = 6$  ns, one more OH-  
44 group attacked the Si atom and finally triggered its complete dissociation. The dissociation  
45 occurred when the maximum distance of a Si atom from its nearest neighbors remained longer  
46 than 3.0 Å.<sup>19</sup> Figure 2F shows the variation of number of dissociated Si atoms in solutions at acidic

(pH 2.2) and basic (pH 10.0) conditions formed by addition of  $H^+$  and  $OH^-$  groups, respectively, compared to a neutral condition (pH 7.0). The results show that the number was increased over the simulation time from 0 ns to 12 ns, while the dissolution was accelerated at higher pH due to the increased concentration of  $OH^-$  groups. It is also anticipated that the enhanced surface porosity would also affect the reaction (dissolution) rate due to the increased contact area between the Si and liquid solution. These findings are consistent with the above-described experimental observations.

**Biocompatibility and controlled drug release.** To evaluate in vivo tissue compatibility, a set of real-time bioluminescence images were captured at 5 h post-injection of the p-Si needles ( $1 \times 1 \text{ cm}^2$ ,  $d = 150 \text{ nm}$ ,  $D = 1 \mu\text{m}$ , and  $L = 50 \mu\text{m}$ ) to the epidermis (on top of the skin; top row) and subcutaneous muscle (under the skin; bottom row) on the backside of mice (Figure 3A). To compare the biocompatibility grade, the experiments were conducted using the p-Si needles built on a medical-grade PVA film (left column; Sigma Aldrich, USA), ones on an industrial-grade PVA film (middle column; Fibre Glast, USA), and a positive control treatment (right column) of phorbol 12-myristate 13-acetate (PMA; 1 mM, 20  $\mu\text{l}$ ; Sigma-Aldrich, USA) that promotes intense local inflammation.<sup>21</sup> Both the epidermis and the subcutaneous muscle showed no evidence of inflammation following the administration of luminol (5-amino-2,3-dihydro-1,4-phthalazinedione) that detects acute inflammation at the implemented sites,<sup>22</sup> whereas acute inflammation appeared in the control mice. Here, the industrial-grade PVA was dissolved within 1 min after the insertion of the p-Si needles into the tissues by applying saline immediately, thereby causing no inflammation. Figure 3B shows in vitro cell viability of human dermal fibroblast (HDF) cells seeded in a 24-well plate (Fisher Scientific, USA) that contains the p-Si needles ( $1 \times 1 \text{ cm}^2$ ,  $d = 150 \text{ nm}$ ,  $D = 2 \mu\text{m}$ , and  $L = 20 \mu\text{m}$ ) and medical-grade PVA film (red bar), as measured using a colorimetric MTT assay kit (3-(4,5-Dimethylthiazol-2-yl)-2,5-diphenyltetrazolium bromide, Sigma-Aldrich, USA). For these tests, the length of the p-Si needles (20  $\mu\text{m}$ -long) was tailored for the HDF cells of which the average diameter is about 20-30  $\mu\text{m}$ . The cell viability remained over 99.3% during the entire period (3 days) of the assay without substantial difference compared to that of the control bare medical-grade PVA film without the p-Si needles (blue bars). Whereas, acute toxicity appeared in the industrial-grade PVA film (green bars) due to the residual ethanol and butanol. Similar results were observed in other control specimens formed by replacing the PVA film with a sheet of water-soluble poly(lactic-co-glycolic acid) (PLGA; 50/50 lactide:glycolide; molecular weight = 30,000-60,000;  $E = 2 \text{ GPa}$ ; Sigma Aldrich, USA), providing the cell viability of > 97.4% (Figure S10).

Covalent conjugation of drug cargos to the surface of the p-Si needles is critical to reliable drug loading and sustained releasing behavior.<sup>9,12</sup> Figure 3C shows representative fluorescence microscopy images (top view) of the p-Si needles where the surface was covalently linked with chemotherapy drug doxorubicin (DOX) via 3-Triethoxysilylpropyl succinic anhydride (TESPSA, Gelest Inc., USA) as a cross-linker. The confocal lens (40 $\times$ ) was focused at the bottom of the p-Si needles, resulting in ring-shaped fluorescence of the DOX. The peak fluorescence intensity of the DOX was observed on the surface of the p-Si needles due to high surface area of the nanopores. Figure 3D shows a three dimensional (3D) confocal image (tilted view) of the p-Si needles upon insertion into a soft agarose gel (2.8% w/v) that provides a comparable mechanical modulus ( $E = \sim 100 \text{ kPa}$ ) to the human tissues ( $E = 80-150 \text{ kPa}$ ). The experiments were performed by gently pressing the PVA film with the p-Si needles ( $1 \times 1 \text{ cm}^2$ ,  $d = 150 \text{ nm}$ ,  $D = 1 \mu\text{m}$ , and  $L = 50 \mu\text{m}$ ) into the agarose gel, followed by the application of saline to completely dissolve the PVA film.

1 The side view of the image (bottom row) highlights that the p-Si needles were embedded inside  
2 the agarose gel through the full length of 50  $\mu\text{m}$ . The larger-field views of the specimen are shown  
3 in Figure S11.

4 Figure 3E shows the total cumulative amount of DOX released from the p-Si needles with  
5 varied surface porosities of 0-60% in PBS (pH 7.4) at 37.5  $^{\circ}\text{C}$ . The corresponding release profiles  
6 as a function of time (up to 100 h) are shown in Figure 3F, exhibiting that rapid release of DOX  
7 occurred within 24 h and then gradually reached a plateau at the predefined doses. The range of  
8 the released doses (18-35  $\mu\text{g}$ ) were comparable to those used in similar studies using polymeric  
9 microneedles.<sup>23,24</sup> Importantly, the released doses remained higher than the half maximal  
10 inhibitory concentration ( $\text{IC}_{50}$ ) value ( $\sim 0.3 \mu\text{g}/\text{ml}$ ) for B16F10 murine melanoma cells and  
11 substantially lower than the lethal dose ( $\text{LD}_{50}$ ) value ( $\sim 192 \mu\text{g}$ ; green dash line) for mice. Figure  
12 3G shows the cumulative release of covalently-linked DOX using different cross-linkers of amide  
13 (red line) and urea (blue line) in PBS (pH 7.4), as compared to that of physically-trapped DOX  
14 (black line). For these tests, the surface porosity of the p-Si needles was fixed at  $\sim 45\%$ . The amide  
15 and urea bonds are well-known to provide strong covalent linkages of the amine group (-NH<sub>2</sub>) of  
16 DOX to the succinic anhydride of 3-(triethoxysilyl) propylsuccinic anhydride (TESPSA) and the  
17 isocyanate (-N=C=O) of 3-isocyanatepropyl triethoxysilane (ICPTS), respectively.<sup>25</sup> The control  
18 physical bond relies on relatively weak Van der Walls force, resulting in rapid and burst release of  
19 drug molecules.<sup>26</sup> The schematic diagrams of these bonding mechanisms are shown in Figure S12.  
20 The highest drug loading capacity occurred in the amide bond ( $\sim 25 \mu\text{g}$ ) followed by the urea bond  
21 ( $\sim 15 \mu\text{g}$ ), both of which were substantially higher than that of the physical trapping ( $\sim 2 \mu\text{g}$ ). These  
22 observations support that the covalently-linked DOX provides strong binding affinity for the  
23 surface of the p-Si needles to form a highly stable complex at physiological pH.<sup>37</sup> The strong  
24 covalent bonding is critical for the sustained release of DOX by allowing the release to occur  
25 predominantly by the gradual dissolution of the p-Si needles. Figure 3H presents the corresponding  
26 release profiles (%) as a function of time (up to 24 h), highlighting the longer-lasting release of the  
27 covalently-linked DOX than counterparts. For instance, more than 80% of the covalently-linked  
28 DOX was released for  $\sim 24$  h (red and blue lines), which was substantially longer than control  
29 specimens with the physically-bonded DOX ( $\sim 8$  h; black line) and conventional polymeric  
30 microneedles (typically, 15 min-2 h; pink-filled area),<sup>27</sup> respectively.

31  
32 **Unobtrusive topical application of p-Si needles.** To illuminate the utility of the p-Si needles in  
33 the envisioned scenarios of transepidermal, transmuscular, and transocular injections, a unit array  
34 of the p-Si needles ( $1 \times 1 \text{ cm}^2$ ,  $d = 150 \text{ nm}$ ,  $D = 1 \mu\text{m}$ , and  $L = 50 \mu\text{m}$ ) with covalently-linked  
35 (amide) fluorescent dyes (DyLight 800, Pierce Thermo Scientific) was introduced to the epidermis,  
36 subcutaneous muscle, and cornea of athymic nude mice *in vivo*. Details of the experimental  
37 procedures are shown in the Materials and Methods section. Figure 4A shows representative  
38 optical images, pointing out the injection sites where the p-Si needles were embedded after the  
39 PVA film was completely dissolved with saline solution. The size of the p-Si needles was much  
40 smaller than that of conventionally-used polymeric microneedles (typically,  $d > 5 \mu\text{m}$ ,  $D > 300$   
41  $\mu\text{m}$ , and  $L > 600 \mu\text{m}$ ),<sup>4,16,28,29</sup> and remained nearly unnoticeable on the tissue surface by visual  
42 observations (Figure S13). This aspect may help reduce the risk of irritation or discomfort  
43 during/after the injection of the p-Si needles. The mice exhibited normal behaviors without  
44 showing any evidence of discomfort against natural movements for the entire period of observation  
45 ( $> 3$  months). Figure 4B shows the corresponding IVIS images, indicating that the fluorescent dyes  
46 were uniformly localized over the irregular surface of the epidermis, subcutaneous muscle, and

1 cornea of the mice, and maintained until the fluorescent dyes were completely absorbed into the  
2 body. Figure S14 shows optical images of a control unit array ( $1 \times 1 \text{ cm}^2$ ) of the p-Si needles  
3 integrated with a flexible, yet non-water-soluble PDMS film (200  $\mu\text{m}$ -thick), which was attached  
4 on the back of a nude mouse. Of note, no wrinkles were observed on the skin over the PDMS film  
5 while other areas of the skin were easily wrinkled according to body movements. These  
6 observations imply that the skin underneath the PDMS film experienced occasional interruptions  
7 or discomforts due to the physical constraints, **highlighting the rationale of eliminating the backing**  
8 **film after complete delivery of the p-Si needles.**

9  
10 **Demonstration on post-surgical melanoma treatments in mice *in vivo*.** Tumor relapse after  
11 surgical resection that often occurs by the outgrowth of residual micrometastases remains a significant  
12 challenge in the treatment.<sup>30</sup> Systemic chemotherapy and radiotherapy are often employed to  
13 prevent the recurrence of residual tumors, but these methods lead to toxic side effects and do not  
14 provide a long-lasting protection unless frequently repeated.<sup>31</sup> Sustained topical delivery of  
15 therapeutic drug cargos with precisely controlled doses for a prolonged time, after surgical  
16 resection, may reduce the risk of tumor relapse with minimal side effects and improved  
17 convenience of patients and healthcare providers.

18 The utility of the p-Si needles in the inhibition of post-surgical residual melanoma was tested  
19 using C57BL/6 mice and syngeneic B16F10 melanoma cells. The mice were subcutaneously  
20 inoculated with  $1 \times 10^6$  B16F10 melanoma cells to mimic a situation where melanoma resection is  
21 incomplete and residual cells are present. Following 2 h of the subcutaneous inoculation, an array  
22 of the p-Si needles ( $1 \times 1 \text{ cm}^2$ ,  $d = 150 \text{ nm}$ ,  $D = 1 \mu\text{m}$ , and  $L = 50 \mu\text{m}$ ) covalently-linked (amide)  
23 with 50  $\mu\text{l}$  of DOX ( $\sim 20 \mu\text{g}$ ) or without DOX (control) were applied to the tumor inoculation site  
24 (Figure 5A). The basic procedure for the injection of the p-Si needles (hereinafter referred to as  
25 “nanoinjection”) is demonstrated in Movie S3 (Supporting Information). A representative  
26 photograph in Figure 5B highlights the nanoinjection site on the shaved skin of a mouse. The  
27 mouse receiving the p-Si needles moved freely without any sign of discomfort (Movie S4,  
28 Supporting Information). Two other control groups of mice were intratumorally administered  
29 using a medical 28G insulin syringe (Fisher Scientific, USA) with a single dose of PBS (50  $\mu\text{l}$ )  
30 and DOX (50  $\mu\text{l}$ ), representing no-treatment control and a conventional bolus injection,  
31 respectively. Figure 5C shows that, in the mice treated with the nanoinjection of DOX, tumor  
32 growth was suppressed over 10 days post-inoculation. In contrast, significant growth of the tumors  
33 occurred in 4 out of 5 mice treated with the control nanoinjection (without DOX), all 5 mice with  
34 the syringe injection of PBS, and 4 out of 5 mice with the syringe injection of DOX during the  
35 same period, followed by rapid increase to reach the endpoint tumor size of  $2,000 \text{ mm}^3$  (Figure  
36 S15).<sup>32</sup> Figure 5D shows the comparisons of the size of the tumors at 10 days post-inoculation. All  
37 of these treatments were well tolerated by the mice with negligible weight loss during the surviving  
38 period (Figure 5E); however, local skin lesions were observed on the mice treated with the syringe  
39 injection of DOX (Figure 5F & Figure S16), which is a typical side effect of the drug.<sup>33</sup> The  
40 superior anti-tumor efficacy of the nanoinjected DOX compared to the bolus-injected DOX with  
41 the same dose is attributable to the prolonged maintenance of effective local concentration based  
42 on the sustained drug release (Figures 3F-H). These findings support that the prolonged release of  
43 DOX to target melanoma sites may lead to enhanced melanoma suppression without adverse  
44 effects compared to burst drug release. This tendency was also observed in previous reports using  
45 polymeric microneedles.<sup>27,34</sup>

1 **CONCLUSION**

2 Controlled cracking at the bottom undercut of vertically-ordered p-Si needles enables their  
3 physical liberation from the rigid Si wafer and subsequent integration with a thin water-soluble  
4 backing film over centimeter-scale areas. The water-soluble film serves as a temporary flexible  
5 holder that can be seamlessly interfaced with the soft, irregular surface of living tissues during the  
6 insertion of the p-Si needles, and then immediately dissolved with saline solution. The nanoscale  
7 sharpened angular tip of the p-Si needles facilitate their penetration into the epidermis,  
8 subcutaneous muscle, and cornea of mice *in vivo* in a minimally invasive manner. The gradual  
9 degradation of the p-Si needles in tissue fluids enables the sustained, long-lasting release of preloaded  
10 drug cargos. *In vivo* evaluations in a murine melanoma model support the potential utility of this  
11 concept in preventing the recurrence of residual melanoma post-surgery. The reported set of  
12 materials, structural designs, and assembly method establishes a technical foundation, which can  
13 be adjusted and tailored for minimally invasive and painless injection of drug cargos through the  
14 cornea for the management of ocular melanomas.<sup>35</sup>

15 **MATERIALS AND METHODS**

16 **Fabrication of the p-Si needles on a Si wafer.** The fabrication began with a bulk Si wafer (p-type;  
17 525  $\mu\text{m}$ -thick; 0-100  $\Omega\cdot\text{cm}$ ) by immersing it in a solution of buffered oxide etch (J. T. Baker  
18 Inc., USA) for 1 min to eliminate the native oxide layer. Following a standard photolithographic  
19 patterning, a deep reactive-ion etching (DRIE) was carried out under a radiofrequency (RF) plasma  
20 power of 450 W and a platen power of 11 W using sulfur hexafluoride (SF<sub>6</sub>) gas with the flow rate  
21 of 85 sccm to create vertically-ordered Si micropillars at a prescribed aspect ratio. The deposition  
22 of (C<sub>x</sub>F<sub>y</sub>)<sub>n</sub> polymer was followed to form a partial passivation layer using octafluorocyclobutane  
23 (C<sub>4</sub>F<sub>8</sub>) gas with the flow rate of 130 sccm under the RF plasma power of 800 W. Additional  
24 isotropic dry etching under the plasma power of 450 W and platen power of 30 W by SF<sub>6</sub> gas with  
25 the flow rate of 85 sccm was conducted to create undercuts at the bottom of the Si micropillars.  
26 The entire specimen was treated with an oxygen (O<sub>2</sub>) plasma (20 sccm, 150 W, 50 mtorr, 15 min),  
27 followed by cleaning with standard piranha solution (75% of sulfuric acid (H<sub>2</sub>SO<sub>4</sub>) and 25% of  
28 hydrogen peroxides (H<sub>2</sub>O<sub>2</sub>)) to eliminate the remaining passivation layer on the surface of the Si  
29 micropillars. Finally, the entire specimen was immersed in a solution of potassium hydroxide  
30 (KOH; 15 weight %; Fisher Scientific, USA) at 25 °C to reduce the overall size of the Si  
31 micropillars down to the nanoscale. The overall size of the miniaturized Si needles was determined  
32 by controlling the molarity of etching solution, temperature, and etching time.<sup>15</sup> The next step  
33 involved the MACE by immersing the specimen in a mixed solution of 20 mM silver nitrate  
34 (AgNO<sub>3</sub>; Sigma-Aldrich, USA) and 49% hydrofluoric acid (HF; J. T. Baker Inc., USA) to form  
35 nanopores on the surface.<sup>36</sup> During the MACE, the overall surface porosity was determined by  
36 controlling the etching time. The specimen was then immersed in a solution of Ag etchant (TFS,  
37 KI-I<sub>2</sub> complex liquid, Transene Inc., USA) for 1 min to remove the remaining Ag residues on the  
38 surface. The surface porosity of the resulting p-Si needles was observed using a high-resolution  
39 SEM (S-4800, Hitachi, Japan), followed by analyzing the surface contrast using a post-image  
40 processing program (Stream Desktop 2.1, Olympus, Japan) in order to quantify the surface  
41 porosity.  
42

43 **Integration of the p-Si needles with a water-soluble film.** The process began by spin-coating a  
44 solution of 10 weight % PVA (Mowiol 4-88; Sigma Aldrich, USA) or 5.5 weight % PLGA  
45 (lactide:glycolide (50:50); Sigma Aldrich, USA) on the as-fabricated p-Si needles on a Si wafer,  
46

1 followed by curing at 70 °C for 30 min. At this stage, the thickness of the water-soluble (PVA or  
2 PLGA) film was determined by adjusting the spin-casting speed (in rpm). The spin-coating was  
3 repeated until the total thickness of the water-soluble film reached about 200 µm for enhancing  
4 mechanical strength. Finally, the film was mechanically peeled using an automated peeling  
5 apparatus (Mark-10, Willrich Precision Instrument) at constant rate of 50 mm/min, causing  
6 cracking at the bottom undercut of the p-Si needles.

7  
8 **Calculation of theoretical strain energy release rate (G).** By measuring the peeling force at low  
9 velocity near zero, the theoretical energy release rate was calculated according to the peeling rate.  
10 In steady-state crack propagation, the strain energy release rate (G) has the following relation by<sup>37</sup>  
11

$$G = \frac{F}{w} \quad (1)$$

12 where F is measured peel force and w is width of the PVA film. By calculating the critical energy  
13 release rate ( $G_0$ ) at the reference velocity ( $v_0$ ) near zero, the theoretical energy release rate can be  
14 determined as power law equation,<sup>38</sup>  
15

$$G = G_0 \left[ 1 + \left( \frac{v}{v_0} \right)^n \right] \quad (2)$$

16 where n is experimentally measured constant. In the peeling tests, the range of the peeling rate of  
17 2.4-200 mm/min, critical energy release rate ( $G_0$ ) of 26.15 J/m<sup>2</sup>, reference velocity ( $v_0$ ) of 2.4  
18 mm/min, and experimental constant (n) of 0.14 were determined.

19 **Finite element analysis (FEA).** The FEA was conducted using the ABAQUS/standard package  
20 to reveal the underlying mechanics of the p-Si needles under peeling process. The deformation of  
21 the p-Si needles and PVA film was modeled by linear elastic behavior with the E of 112.4 GPa  
22 and 3.4 GPa, respectively.<sup>39</sup> The materials were modeled by 8 nodes solid elements (C<sub>3</sub>D<sub>8</sub>R). The  
23 displacement at constant peeling rate was applied on the top of the PVA film while a tie constraint  
24 was defined at the interface between the p-Si needles and PVA film.

25 **Loading of DOX on the surface of the p-Si needles.** The process began by washing the as-  
26 fabricated p-Si needles on a Si wafer with distilled (DI) water, followed by thorough drying with  
27 nitrogen (N<sub>2</sub>) gas. The cleaned p-Si needles were immersed in a solution of 3-Triethoxysilylpropyl  
28 succinic anhydride (TESPSA; Gelest Inc., USA) for 2 h to functionalize the surface with amide.<sup>40</sup>  
29 Alternatively, the p-Si needles were immersed in a solution of 3-Triethoxysilylpropyl isocyanate  
30 (ICPTS; Sigma-Aldrich, USA) for 2 h to functionalize the surface with urea.<sup>41</sup> The p-Si needles  
31 were then rinsed with ethanol and then baked at 120 °C for 1 h, followed by immersing in a solution  
32 of DOX (0.5 mg/ml; Sigma-Aldrich, USA) for 24 h at room temperature. To prepare the control  
33 specimens with physically-trapped DOX, the as-fabricated p-Si needles were immersed in a  
34 solution of DOX without undergoing any treatment on the surface. The prepared specimens were  
35 dried by N<sub>2</sub> gas and stored under an inert atmosphere.

36  
37 **Measurements of cumulative DOX release.** The p-Si needles loaded with DOX were immersed  
38 in 12-well plate with 4 ml of PBS (pH 7.4 or pH 10.0; Sigma-Aldrich, USA) at 37.5 °C. At the  
39

1 predetermined time intervals, the specimens were sampled and the PBS solution was refreshed. A  
2 100  $\mu$ l of the sampled solution was transferred to a 96-well plate, and the fluorescent intensity was  
3 measured with a plate reader (Synergy Neo Plate Reader, BioTek Instruments). The concentration  
4 of the released DOX was determined according to the fluorescent intensity measured with the  
5 excitation and emission at 480 nm and 600 nm, respectively.<sup>42</sup>

6  
7 **Molecular dynamics (MD) simulations.** The MD simulations were conducted to model atomic  
8 scale chemical interactions of Si with H<sub>2</sub>O and the associated dissolution dynamics with the Reaxff  
9 potential<sup>43</sup> using a large-scale atomic/molecular massively parallel simulator (LAMMPS) package.  
10 In these simulations, Si, O, and H were used for the atomic elements.<sup>44</sup> The initial systems included  
11 a Si layer with the thickness of 1.2 nm, which was solvated by a box of H<sub>2</sub>O with 3090 water  
12 molecules. Periodic boundary conditions were used in all directions. The temperature of the system  
13 was maintained at 300 K using the Nose-Hoover thermostat, and the time step was selected to be  
14 0.1 fs, in order to ensure the capture of chemical reaction events between the Si and H<sub>2</sub>O species.  
15

16 **Cell viability tests.** For the MTT assay, approximately  $5 \times 10^4$  human dermal fibroblast (HDF)  
17 cells were seeded on a specimen in a 24-well plate and then incubated for 24 h, 48 h, and 72 h. At  
18 each measurement point, 200  $\mu$ l of MTT solution ((3-(4,5-dimethylthiazol-2-yl)-2,5-diphenyltetrazolium bromide); Sigma-Aldrich, USA) was added to the wells and incubated for 4 h. The cell medium was removed, and 400  $\mu$ l of dimethyl sulfoxide (C<sub>2</sub>H<sub>6</sub>OH; Sigma-Aldrich, USA) was added to dissolve precipitated formazan. A 100  $\mu$ l of the solution was transferred to a 96-well plate and measured using a microplate reader (SpectraMax Plus 384 reader, Molecular Devices, USA) at 570 nm.  
24

25 **Acute inflammation tests in vivo.** All of these animal studies were approved by the Purdue  
26 Animal Care and Use Committee (PACUC; #1612001512) for the care and use of laboratory  
27 animals. Female athymic nude mice (5-6 weeks old; NCr-Fox1nu, Charles River Laboratories,  
28 USA) were used in the acute inflammation tests in vivo. As a positive control, 40  $\mu$ l of PMA (100  $\mu$ M; Sigma-Aldrich, USA) was rubbed on the epidermis and subcutaneous muscle to induce acute  
29 inflammation.<sup>34</sup> The p-Si needles on a PVA film were gently applied to target sites with firm  
30 compression. The backing film was then completely dissolved by applying a saline-moistened  
31 cotton swab. Following 5 h of the implementation, 100  $\mu$ l of luminol sodium salt (200 mg/kg; Sigma-Aldrich, USA) was administered by the intraperitoneal nanoinjection. Then, the mice were  
32 anesthetized with compressed air containing 2.5% isoflurane with a Classic T3 isoflurane  
33 vaporizer (Smith Medical, Dublin, OH). Bioluminescence images were acquired using an IVIS  
34 Lumina II imaging system (Caliper Life Sciences, USA) for 3 min of the exposure time at the  
35 F/stop and binning of 1 and 4, respectively.  
38

39 **IVIS imaging in vivo.** All of these animal studies were approved by the Purdue Animal Care and  
40 Use Committee (PACUC; #1612001512). The p-Si needles with covalently-linked (amide)  
41 DyLight 800 dyes were placed either on the epidermis, subcutaneous muscle, or cornea of mice  
42 (5-6 weeks old; NCr-Fox1nu, Charles River Laboratories, USA) with firm compression. For the  
43 transmuscular nanoinjection, 250 mg/kg of avertin (Sigma-Aldrich, USA) was administrated by  
44 an intraperitoneal injection to anesthetize mice, followed by careful incision of the skin with  
45 surgical scissors. The incisional site was then sutured using a surgical needle and thread. The mice  
46 were anesthetized with inhaled isoflurane anesthesia with a Classic T3 isoflurane vaporizer (Smith

1 Medical, Dublin, OH) and exposed to 2.5% isoflurane delivered in O<sub>2</sub> (2 litters/min) within a 1-litter induction chamber. The fluorescence of the injection site was measured using an IVIS Lumina II imaging system (Caliper Life Sciences, USA) at the day 0, 1, and 2 with the exposure time of 1 s each using a 150 W quartz halogen lamp, and then filtered using an indocyanine green (ICG) excitation and emission filters with the wavelengths of 710-760 nm and 810-875 nm, respectively. The data analysis was performed using the Living Image software (version 4.4, PerkinElmer Inc).

9 **Demonstration in a murine melanoma model.** All of these animal procedures were approved by  
10 the Purdue Animal Care and Use Committee (PACUC; #1503001212). Male C57BL/6 mice (8-10  
11 weeks old; Envigo, USA) were acclimatized for at least 1 week prior to the procedures. The p-Si  
12 needles were sterilized by an ultraviolet (UV) illumination (254 nm) for 30 min. 10<sup>6</sup> B16F10  
13 melanoma cells (ATCC; Manassas, VA, USA) were subcutaneously inoculated in the bottom flank  
14 of the right hind leg of each mouse. After approximately 2 h, the inoculation site was treated with  
15 the nanoinjection of the covalently-linked (amide) DOX (~20 µg) and the control nanoinjection  
16 (without DOX). For comparison, two other control groups of mice were intratumorally  
17 administered using a medical 28G insulin syringe (Fisher, USA) with a single dose of PBS (50 µl)  
18 and DOX (20 µg in 50 µl), respectively. The length (L) and width (W) of each tumor were  
19 monitored every day using a digital caliper (Thorlabs Digital Calipers, Thorlabs Inc, USA), and  
20 the volume (V) was calculated according to an ellipsoid formula: V = (L×W<sup>2</sup>)/2. The body weight  
21 of the mice was monitored every other day.

22  
23 **Data availability.** The data that support the plots in this paper and other finding of this study are  
24 available from the corresponding authors upon reasonable request.

## 26 ASSOCIATED CONTENT

### 27 Supporting Information.

28 SEM images of the p-Si needles fabricated on a donor Si wafer with varied sizes (Figure S1); SEM  
29 images of the PVA film coated on the p-Si needles at varied spin-casting speeds (Figure S2); SEM  
30 images of a donor Si wafer and receiver PVA film (Figure S3); SEM images of the p-Si needles  
31 with varied surface porosities (Figure S4); Time-dependent optical images of a yellow-colored  
32 PVA film (Figure S5); Optical image and the corresponding measurement results of the peeling of  
33 the p-Si needles (Figure S6); FEA results displaying the distribution of the principal strains for the  
34 p-Si needle during peeling process (Figure S7); Representative SEM image displaying the  
35 compressed marks leftover on the surface of a receiver PVA film peeled out of optimal conditions  
36 (Figure S8); SEM images of the p-Si needles immersed in 50 ml of PBS (pH 7.4) at 37.5 °C for  
37 90 days (Figure S9); Photograph and SEM image of the p-Si needles built on a water-soluble  
38 PLGA film and the corresponding results of MTT assay for the cytotoxicity test of HDF cells  
39 (Figure S10); Microscope images of the p-Si needles penetrated into a 2.8% (w/v) agarose gel  
40 (Figure S11); Schematic diagrams of the amide, urea, and physical bonds of DOX to the surface  
41 of the p-Si needles (Figure S12); Enlarged optical images of the epidermis, subcutaneous muscle,  
42 and cornea of mice receiving the p-Si needles (Figure S13); Optical images of a nude mouse worn  
43 with the control p-Si needles built on a PDMS film on the backside (Figure S14); Measurement  
44 results of the tumor size (Figure S15); Enlarged optical images of the treated sites of the mice at  
45 10 days post-injection (Figure S16); Visual observation (16× speed) of a yellow-colored PVA  
46 immersed in a solution of PBS (pH 7.4) at 37.5 °C (Movie S1); Real-time demonstration of the

1 automated peeling of the p-Si needles from the donor Si wafer (Movie S2); Demonstration (26×  
2 speed) of the nanoinjection of DOX to the shaved skin of a mouse after 2 h of subcutaneous  
3 inoculation with  $1 \times 10^6$  B16F10 melanoma cells (Movie S3); Visual observation (2× speed) of a  
4 mouse receiving an array (1×1 cm<sup>2</sup>) of the p-Si needles with covalently-linked (amide) DOX on  
5 the back side (Movie S4).

## 7 **AUTHOR INFORMATION**

### 8 **Corresponding Authors**

9 \*Email: [yyeo@purdue.edu](mailto:yyeo@purdue.edu) (Y.Y.)

10 \*Email: [dongrip@hanyang.ac.kr](mailto:dongrip@hanyang.ac.kr) (D.R.K.)

11 \*Email: [lee2270@purdue.edu](mailto:lee2270@purdue.edu) (C.H.L.)

### 13 **Author Contributions**

14 #H.K., H.L. contributed equally to this work.

## 16 **ACKNOWLEDGMENT**

17 C.H.L. acknowledges funding support from the Asian Office of Aerospace Research &  
18 Development (AOARD: FA2386-16-1-4105; Program manager: Dr. Tony Kim) and the Air Force  
19 Office of Scientific Research (AFOSR: FA2386-18-1-40171; Program manager: Dr. Tony Kim).  
20 D.R.K. acknowledges funding support from the International Research and Development Program  
21 (NRF-2018K1A3A1A32055469) and the Basic Science Research Program (NRF-  
22 2018R1C1B6007938) through the National Research Foundation of Korea (NRF) funded by the  
23 Ministry of Science and ICT of Korea. Y.Y. acknowledges funding support from the National  
24 Institute of Health (NIH: R01 CA199663). B. X. acknowledges funding support on  
25 chemomechanics of reactive MD simulations from National Science Foundation (NSF-CMMI-  
26 1728149)

## 27 **REFERENCES**

1. Simoes, M. C. F.; Sousa, J. J. S.; Pais, A., Skin Cancer and New Treatment Perspectives: A  
2 review. *Cancer Lett.* **2015**, *357*, 8-42.
3. Perera, E.; Gnaneswaran, N.; Jennens, R.; Sinclair, R., Malignant Melanoma. *Healthcare* **2014**,  
4 2, 1-19.
5. Prausnitz, M. R.; Langer, R., Transdermal Drug Delivery. *Nat. Biotechnology* **2008**, *26*, 1261-  
6 1268.
7. Li, W.; Terry, R. N.; Tang, J.; Feng, M. H. R.; Schwendeman, S. P.; Prausnitz, M. R., Rapidly  
8 Separable Microneedle Patch for the Sustained Release of a Contraceptive. *Nat. Biomed. Eng.*  
9 **2019**, *3*, 220-230.
10. Gopal, S.; Chiappini, C.; Penders, J.; Leonardo, V.; Seong, H.; Rothery, S.; Korchev, Y.;  
11 Shevchuk, A.; Stevens, M. M., Porous Silicon Nanoneedles Modulate Endocytosis to Deliver  
12 Biological Payloads. *Adv. Mater.* **2019**, *31*, 1-8.
13. Chiappini, C.; De Rosa, E.; Martinez, J.; Liu, X.; Steele, J.; Stevens, M.; Tasciotti, E.,  
14 Biodegradable Silicon Nanoneedles Delivering Nucleic Acids Intracellularly Induce Localized  
15 in Vivo Neovascularization. *Nat. Mater.* **2015**, *14*, 532-539.
16. Chiappini, C.; Martinez, J.; De Rosa, E.; Almeida, C.; Tasciotti, E.; Stevens, M.,  
17 Biodegradable Nanoneedles for Localized Delivery of Nanoparticles in Vivo: Exploring the  
18 Biointerface. *ACS Nano* **2015**, *9*, 5500-5509.

1 8. Fang, Y.; Jiang, Y. W.; Ledesrna, H. A.; Yi, J. S.; Gao, X.; Weiss, D. E.; Shi, F. Y.; Tian, B.  
2 Z., Texturing Silicon Nanowires for Highly Localized Optical Modulation of Cellular  
3 Dynamics. *Nano Lett.* **2018**, 18, 4487-4492.

4 9. Anglin, E. J.; Cheng, L. Y.; Freeman, W. R.; Sailor, M. J., Porous Silicon in Drug Delivery  
5 Devices and Materials. *Adv. Drug Delivery Rev.* **2008**, 60, 1266-1277.

6 10. Lee, Y. K.; Yu, K. J.; Song, E. M.; Farimani, A. B.; Vitale, F.; Xie, Z. Q.; Yoon, Y.; Kim, Y.;  
7 Richardson, A.; Luan, H. W.; Wu, Y. X.; Xie, X.; Lucas, T. H.; Crawford, K.; Mei, Y. F.;  
8 Feng, X.; Huang, Y. G.; Litt, B.; Aluru, N. R.; Yin, L.; Rogers, J. A., Dissolution of  
9 Monocrystalline Silicon Nanomembranes and Their Use as Encapsulation Layers and  
10 Electrical Interfaces in Water-Soluble Electronics. *ACS Nano* **2017**, 11, 12562-12572.

11 11. Hwang, S.; Park, G.; Edwards, C.; Corbin, E.; Kang, S.; Cheng, H.; Song, J.; Kim, J.; Yu, S.;  
12 Ng, J.; Lee, J.; Kim, J.; Yee, C.; Bhaduri, B.; Su, Y.; Omennetto, F.; Huang, Y.; Bashir, R.;  
13 Goddard, L.; Popescu, G.; Lee, K.; Rogers, J., Dissolution Chemistry and Biocompatibility of  
14 Single-Crystalline Silicon Nanomembranes and Associated Materials for Transient  
15 Electronics. *Acs Nano* **2014**, 8, 5843-5851.

16 12. Santos, H. A.; Makila, E.; Airaksinen, A. J.; Bimbo, L. M.; Hirvonen, J., Porous Silicon  
17 Nanoparticles for Nanomedicine: Preparation and Biomedical Applications. *Nanomedicine*  
18 **2014**, 9, 535-554.

19 13. Abbott, J.; Ye, T. Y.; Ham, D.; Park, H., Optimizing Nanoelectrode Arrays for Scalable  
20 Intracellular Electrophysiology. *Acc. Chem. Res.* **2018**, 51, 600-608.

21 14. Jovanovic, P.; Mihajlovic, M.; Djordjevic-Jocic, J.; Vlajkovic, S.; Cekic, S.; Stefanovic, V.,  
22 Ocular Melanoma: An Overview of the Current Status. *Int. J. Clin. Exp. Pathol.* **2013**, 6, 1230-  
23 1244.

24 15. Kim, H.; Jang, H.; Kim, B.; Kim, M. K.; Wie, D. S.; Lee, H. S.; Kim, D. R.; Lee, C. H., Flexible  
25 Elastomer Patch with Vertical Silicon Nanoneedles for Intracellular and Intratissue  
26 Nanoinjection of Biomolecules. *Sci. Adv.* **2018**, 4, 1-8.

27 16. Lim, J.; Tahk, D.; Yu, J.; Min, D. H.; Jeon, N. L., Design Rules for a Tunable Merged-Tip  
28 Microneedle. *Microsyst. & Nanoeng.* **2018**, 4, 1-10.

29 17. Meitl, M.; Zhu, Z.; Kumar, V.; Lee, K.; Feng, X.; Huang, Y.; Adesida, I.; Nuzzo, R.; Rogers,  
30 J., Transfer Printing by Kinetic Control of Adhesion to an Elastomeric Stamp. *Nat. Mater.*  
31 **2006**, 5, 33-38.

32 18. Wang, L.; Gao, Y.; Dai, F. Q.; Kong, D. Y.; Wang, H. C.; Sun, P. C.; Shi, Z.; Sheng, X.; Xu,  
33 B. X.; Yin, L., Geometrical and Chemical-Dependent Hydrolysis Mechanisms of Silicon  
34 Nanomembranes for Biodegradable Electronics. *ACS Appl. Mater. Interfaces* **2019**, 11, 18013-  
35 18023.

36 19. Yin, L.; Farimani, A.; Min, K.; Vishal, N.; Lam, J.; Lee, Y.; Aluru, N.; Rogers, J., Mechanisms  
37 for Hydrolysis of Silicon Nanomembranes as Used in Bioresorbable Electronics. *Adv. Mater.*  
38 **2015**, 27, 1-8.

39 20. Chang, J. K.; Emon, M. A. B.; Li, C. S.; Yang, Q. S.; Chang, H. P.; Yang, Z. J.; Wu, C. I.;  
40 Saif, M. T.; Rogers, J. A., Cytotoxicity and in Vitro Degradation Kinetics of Foundry-  
41 Compatible Semiconductor Nanomembranes and Electronic Microcomponents. *ACS Nano*  
42 **2018**, 12, 9721-9732.

43 21. Muller, A. J.; Sharma, M. D.; Chandler, P. R.; DuHadaway, J. B.; Everhart, M. E.; Johnson,  
44 B. A.; Kahler, D. J.; Pihkala, J.; Soler, A. P.; Munn, D. H.; Prendergast, G. C.; Mellor, A. L.,  
45 Chronic Inflammation that Facilitates Tumor Progression Creates Local Immune Suppression

1 by Inducing Indoleamine 2,3 Dioxygenase. *Proc. Natl. Acad. Sci. U. S. A* **2008**, 105, 17073-17078.

2 22. Gross, S.; Gammon, S. T.; Moss, B. L.; Rauch, D.; Harding, J.; Heinecke, J. W.; Ratner, L.;  
3 Piwnica-Worms, D., Bioluminescence Imaging of Myeloperoxidase Activity in Vivo. *Nat. Med.* **2009**, 15, 455-461.

4 23. Pei, P.; Yang, F.; Liu, J. X.; Hu, H. R.; Du, X. Y.; Hanagata, N.; Zhao, S. C.; Zhu, Y. F.,  
5 Composite-Dissolving Microneedle Patches for Chemotherapy and Photothermal Therapy in  
6 Superficial Tumor Treatment. *Biomater. Sci.* **2018**, 6, 1414-1423.

7 24. Ahmed, K. S.; Shan, X.; Mao, J.; Qiu, L.; Chen, J., Derma roller (R) Microneedles-Mediated  
8 Transdermal Delivery of Doxorubicin and Celecoxib Co-Loaded Liposomes for Enhancing the  
9 Anticancer Effect. *Mater. Sci. Eng., C* **2019**, 99, 1448-1458.

10 25. Wang, Z. H.; Gangarapu, S.; Escorihuela, J.; Fei, G. X.; Zuilhof, H.; Xia, H. S., Dynamic  
11 Covalent Urea Bonds and Their Potential for Development of Self-Healing Polymer Materials.  
12 *J. Mater. Chem. A* **2019**, 7, 15933-15943.

13 26. Wu, E. C.; Park, J.-H.; Park, J.; Segal, E.; Cunin, F.; Sailor, M. J., Oxidation-Triggered Release  
14 of Fluorescent Molecules or Drugs from Mesoporous Si Microplarticles. *ACS Nano* **2008**, 2,  
15 2401-2409.

16 27. Bhatnagar, S.; Bankar, N. G.; Kulkarni, M. V.; Venuganti, V. V. K., Dissolvable Microneedle  
17 Patch Containing Doxorubicin and Docetaxel is Effective in 4T1 Xenografted Breast Cancer  
18 Mouse Model. *Int. J. Pharm.* **2019**, 556, 263-275.

19 28. Chen, M. C.; Lin, Z. W.; Ling, M. H., Near-Infrared Light-Activatable Microneedle System  
20 for Treating Superficial Tumors by Combination of Chemotherapy and Photothermal Therapy.  
21 *ACS Nano* **2016**, 10, 93-101.

22 29. Sullivan, S. P.; Koutsonanos, D. G.; Martin, M. D.; Lee, J. W.; Zarnitsyn, V.; Choi, S. O.;  
23 Murthy, N.; Compans, R. W.; Skountzou, I.; Prausnitz, M. R., Dissolving Polymer  
24 Microneedle Patches for Influenza Vaccination. *Nat. Med.* **2010**, 16, 1-7.

25 30. Chen, Q.; Wang, C.; Zhang, X.; Chen, G.; Hu, Q.; Li, H.; Wang, J.; Wen, D.; Zhang, Y.; Lu,  
26 Y.; Yang, G.; Jiang, C.; Wang, J.; Dotti, G.; Gu, Z., In Situ Sprayed Bioresponsive  
27 Immunotherapeutic Gel for Post-Surgical Cancer Treatment. *Nat. Nanotechnol.* **2019**, 14, 89-98.

28 31. Albain, K. S.; Swann, R. S.; Rusch, V. W.; Turrisi, A. T., III; Shepherd, F. A.; Smith, C.; Chen,  
29 Y.; Livingston, R. B.; Feins, R. H.; Gandara, D. R.; Fry, W. A.; Darling, G.; Johnson, D. H.;  
30 Green, M. R.; Miller, R. C.; Ley, J.; Sause, W. T.; Cox, J. D., Radiotherapy Plus Chemotherapy  
31 with or without Surgical Resection for Stage III Non-Small-Cell Lung Cancer: A Phase III  
32 Randomised Controlled Trial. *Lancet* **2009**, 374, 379-386.

33 32. Xu, J.; Lee, S. S.-Y.; Seo, H.; Pang, L.; Jun, Y.; Zhang, R.-Y.; Zhang, Z.-Y.; Kim, P.; Lee, W.;  
34 Kron, S. J.; Yeo, Y., Quinic Acid-Conjugated Nanoparticles Enhance Drug Delivery to Solid  
35 Tumors via Interactions with Endothelial Selectins. *Small* **2018**, 14, 1-16.

36 33. Courtenay, A. J.; McCrudden, M. T. C.; McAvoy, K. J.; McCarthy, H. O.; Donnelly, R. F.,  
37 Microneedle-Mediated Transdermal Delivery of Bevacizumab. *Mol. Pharm.* **2018**, 15, 3545-3556.

38 34. Kubicka-Wolkowska, J.; Kedzierska, M.; Lisik-Habib, M.; Potemski, P., Skin Toxicity in a  
39 Patient with Ovarian Cancer Treated with Pegylated Liposomal Doxorubicin: A Case Report  
40 and Review of the Literature. *Oncol. Lett.* **2016**, 12, 5332-5334.

41 35. Sassalos, T. M.; Paulus, Y. M., Prefilled Syringes for Intravitreal Drug Delivery. *Clin.  
42 Ophthalmol.* **2019**, 13, 701-706.

1 36. Han, H.; Huang, Z.; Lee, W., Metal-Assisted Chemical Etching of Silicon and Nanotechnology  
2 Applications. *Nano Today* **2014**, 9, 271-304.

3 37. Feng, X.; Meitl, M. A.; Bowen, A. M.; Huang, Y.; Nuzzo, R. G.; Rogers, J. A., Competing  
4 Fracture in Kinetically Controlled Transfer Printing. *Langmuir* **2007**, 23, 12555-12560.

5 38. Chen, H.; Feng, X.; Huang, Y.; Huang, Y. G.; Rogers, J. A., Experiments and Viscoelastic  
6 Analysis of Peel Test with Patterned Strips for Applications to Transfer Printing. *J. Mech.  
7 Phys. Solids* **2013**, 61, 1737-1752.

8 39. Ryu, S.; Xiao, J.; Il Park, W.; Son, K.; Huang, Y.; Paik, U.; Rogers, J., Lateral Buckling  
9 Mechanics in Silicon Nanowires on Elastomeric Substrates. *Nano Lett.* **2009**, 9, 3214-3219.

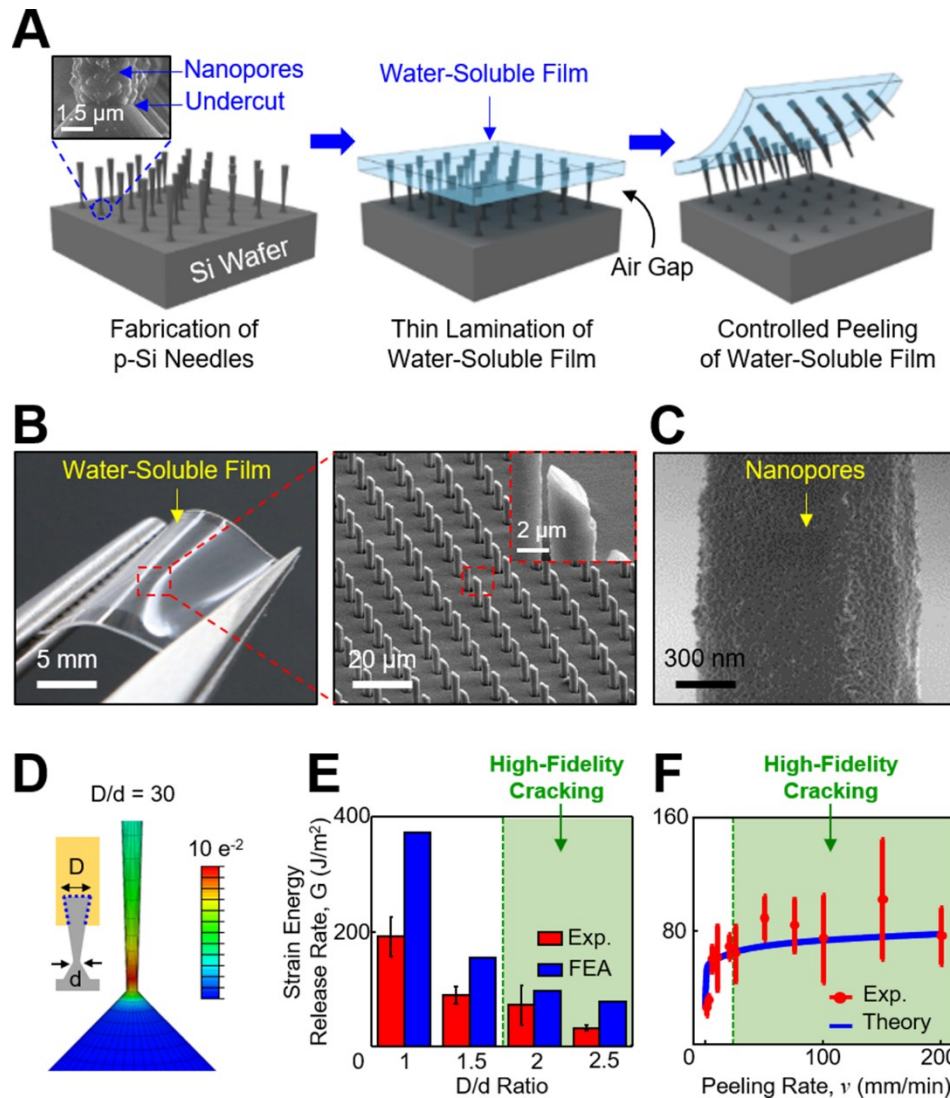
10 40. Gang, A.; Gabernet, G.; Renner, L. D.; Baraban, L.; Cuniberti, G., A Simple Two-Step Silane-  
11 Based (bio-) Receptor Molecule Immobilization without Additional Binding Site Passivation.  
12 *RSC Adv.* **2015**, 5, 35631-35634.

13 41. Escorihuela, J.; Jose Banuls, M.; Garcia Castello, J.; Toccafondo, V.; Garcia-Ruperez, J.;  
14 Puchades, R.; Maquieira, A., Chemical Silicon Surface Modification and Bioreceptor  
15 Attachment to Develop Competitive Integrated Photonic Biosensors. *Anal. Bioanal. Chem.*  
16 **2012**, 404, 2831-2840.

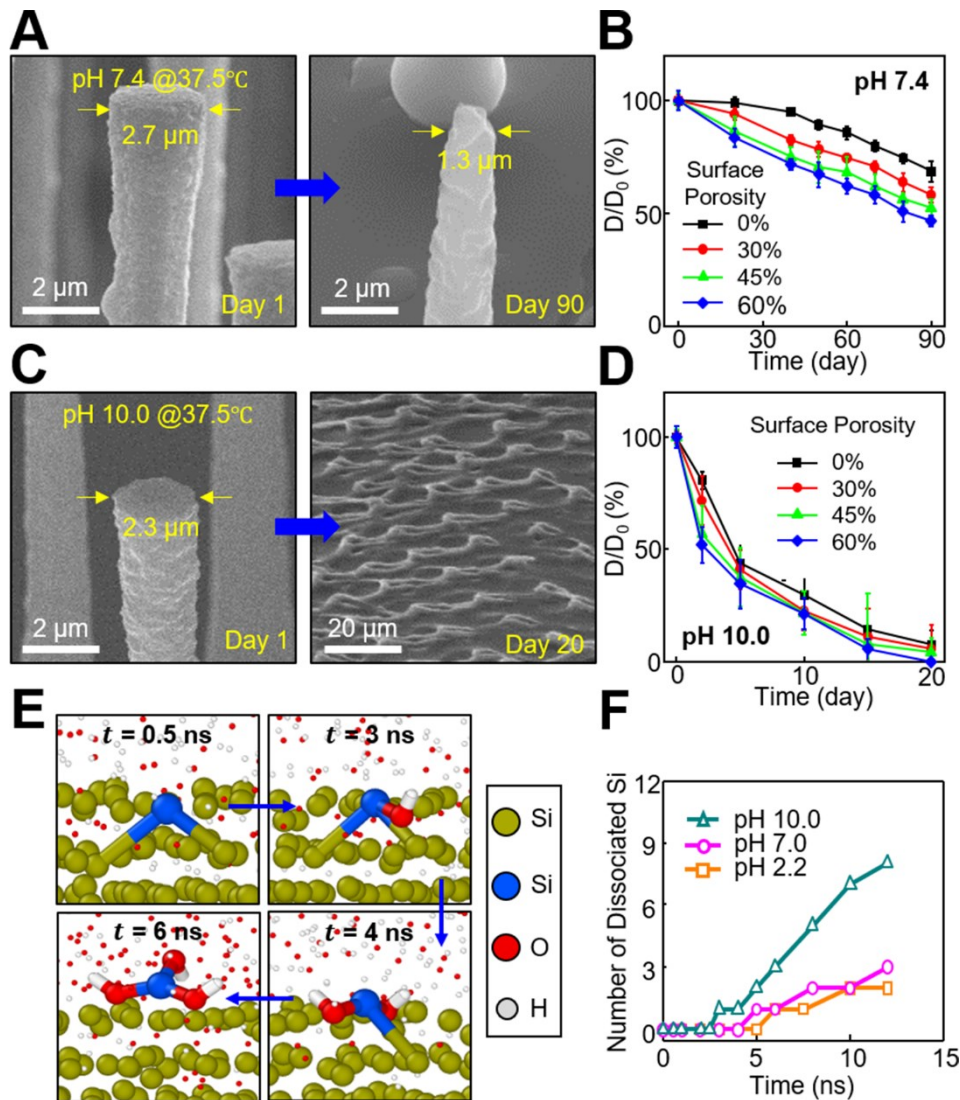
17 42. Shah, S.; Chandra, A.; Kaur, A.; Sabnis, N.; Lacko, A.; Gryczynski, Z.; Fudala, R.;  
18 Gryczynski, I., Fluorescence Properties of Doxorubicin in PBS Buffer and PVA Films. *J.  
19 Photochem. Photobiol. B* **2017**, 170, 65-69.

20 43. Zhang, Y.; Kim, B. O. O.; Gao, Y.; Wie, D. S.; Lee, C. H.; Xu, B. X., Chemomechanics of  
21 Transfer Printing of Thin Films in a Liquid Environment. *Int. J. Solids Struct.* **2019**, 180, 30-  
22 44.

23 44. Fogarty, J. C.; Aktulga, H. M.; Grama, A. Y.; van Duin, A. C. T.; Pandit, S. A., A Reactive  
24 Molecular Dynamics Simulation of the Silica-Water Interface. *J. Chem. Phy.* **2010**, 132, 1-10.



1  
2 **Figure 1. Design principle and fabrication process.** (A) Schematic illustrations for the  
3 construction of the p-Si needles on a water-soluble backing. The inset image highlights the bottom  
4 undercut and nanopores at the bottom and on the surface of the p-Si needles, respectively. (B)  
5 Optical images of the p-Si needles integrated with a PVA film. The inset image highlights the  
6 sharpened angular tip of the p-Si needles. (C) SEM image of the nanopores formed on the surface  
7 of the p-Si needles. (D) Representative FEA results showing the distribution of principal strains  
8 along the p-Si needle during constant peeling. (E) Experimental and FEA results for the effect of  
9 D/d ratio on strain energy release rate (G). (F) Experimental and theoretical results for the effect  
10 of peeling rate ( $v$ ) on G.  
11



1  
 2 **Figure 2. Degradation of the p-Si needles in biofluids.** (A) SEM images of the p-Si needles at 1  
 3 day (left image) and 90 days (right image) after immersing in 50 ml of PBS (pH 7.4) at 37.5 °C.  
 4 (B) Measurement results of  $D/D_0$  ratio (%) obtained from the p-Si needles with varied surface  
 5 porosities of 0% (black), 30% (red), 45% (green), and 60% (blue). (C) SEM images of the p-Si  
 6 needles at 1 day (left image) and 20 days (right image) after immersing in 50 ml of PBS (pH 10.0)  
 7 at 37.5 °C. (D) Measurement results of  $D/D_0$  ratio (%) obtained from the p-Si needles with varied  
 8 surface porosities. (E) Snapshot images of MD simulation at different time frames. (F) Results of  
 9 the number of dissociated Si atoms in solutions at acidic (pH 2.2) and basic (pH 10.0) conditions  
 10 formed by the addition of  $H^+$  and  $OH^-$  groups, respectively, compared to a neutral condition (pH  
 11 7.0).  
 12

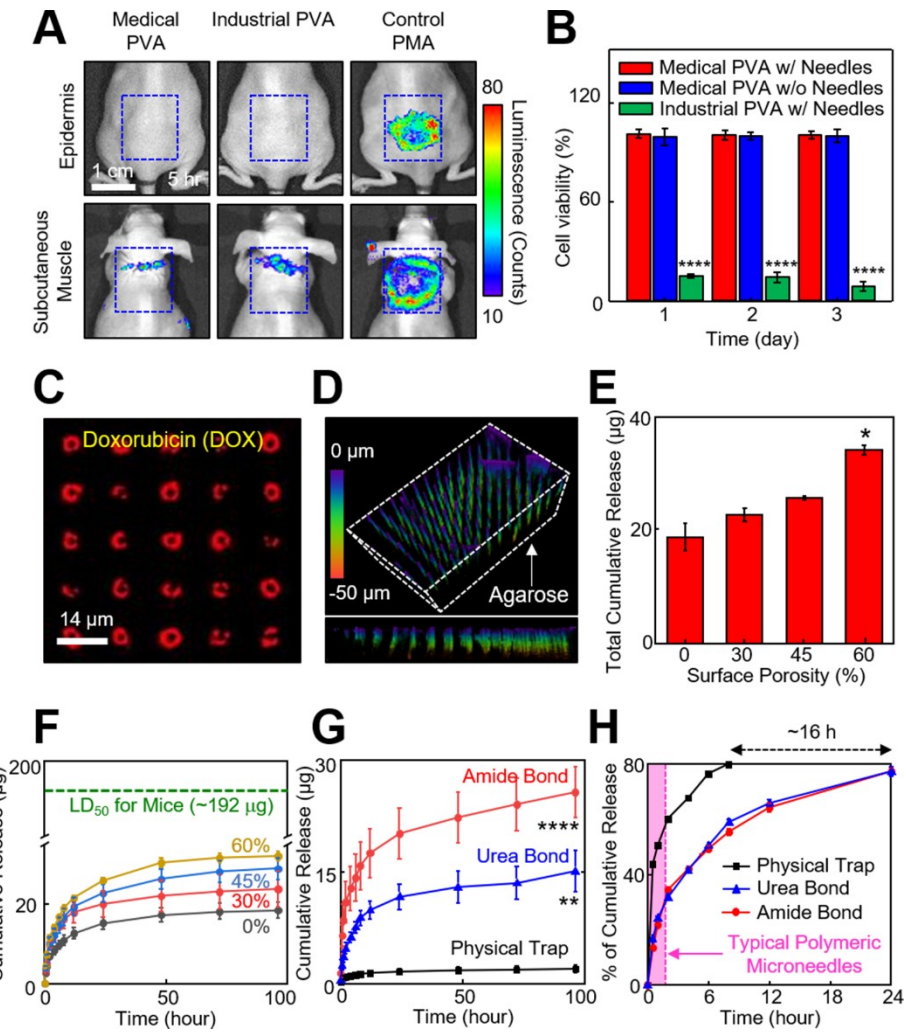
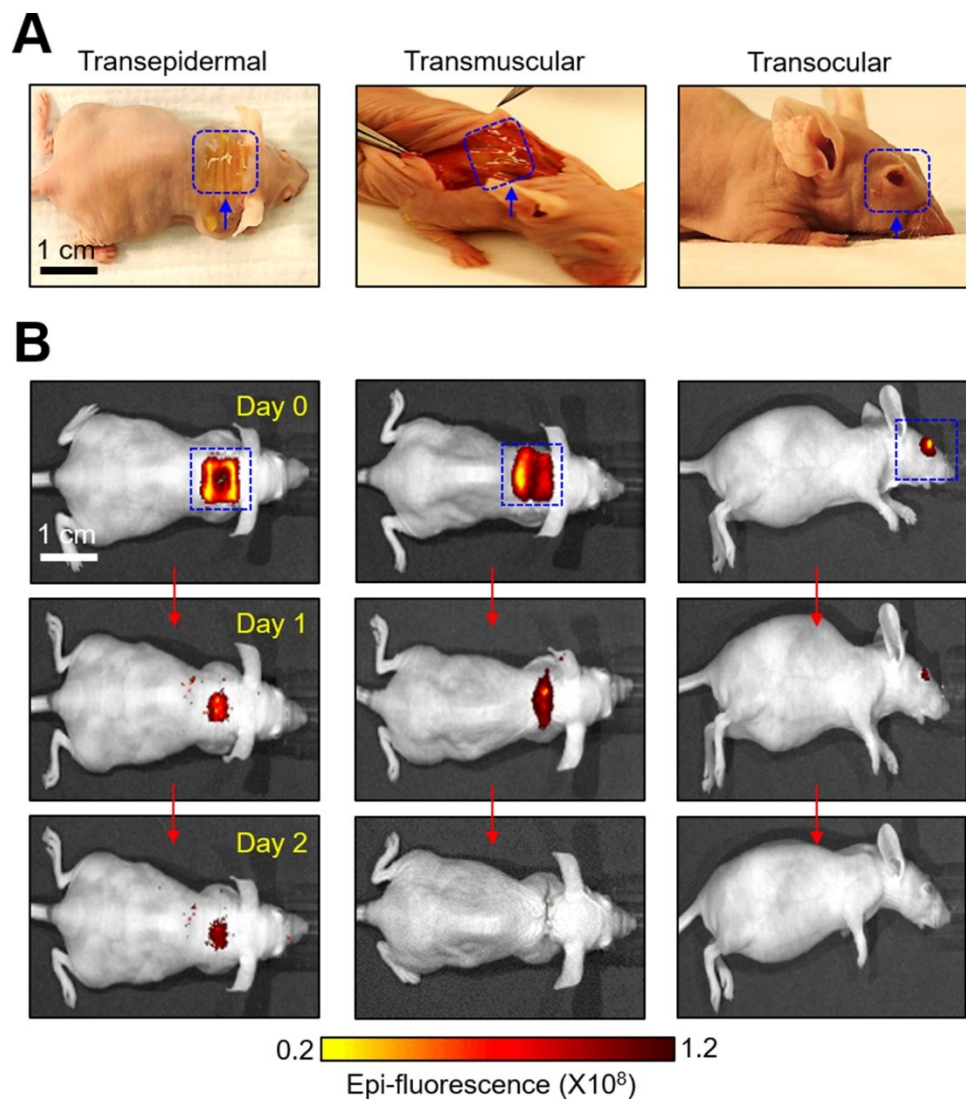
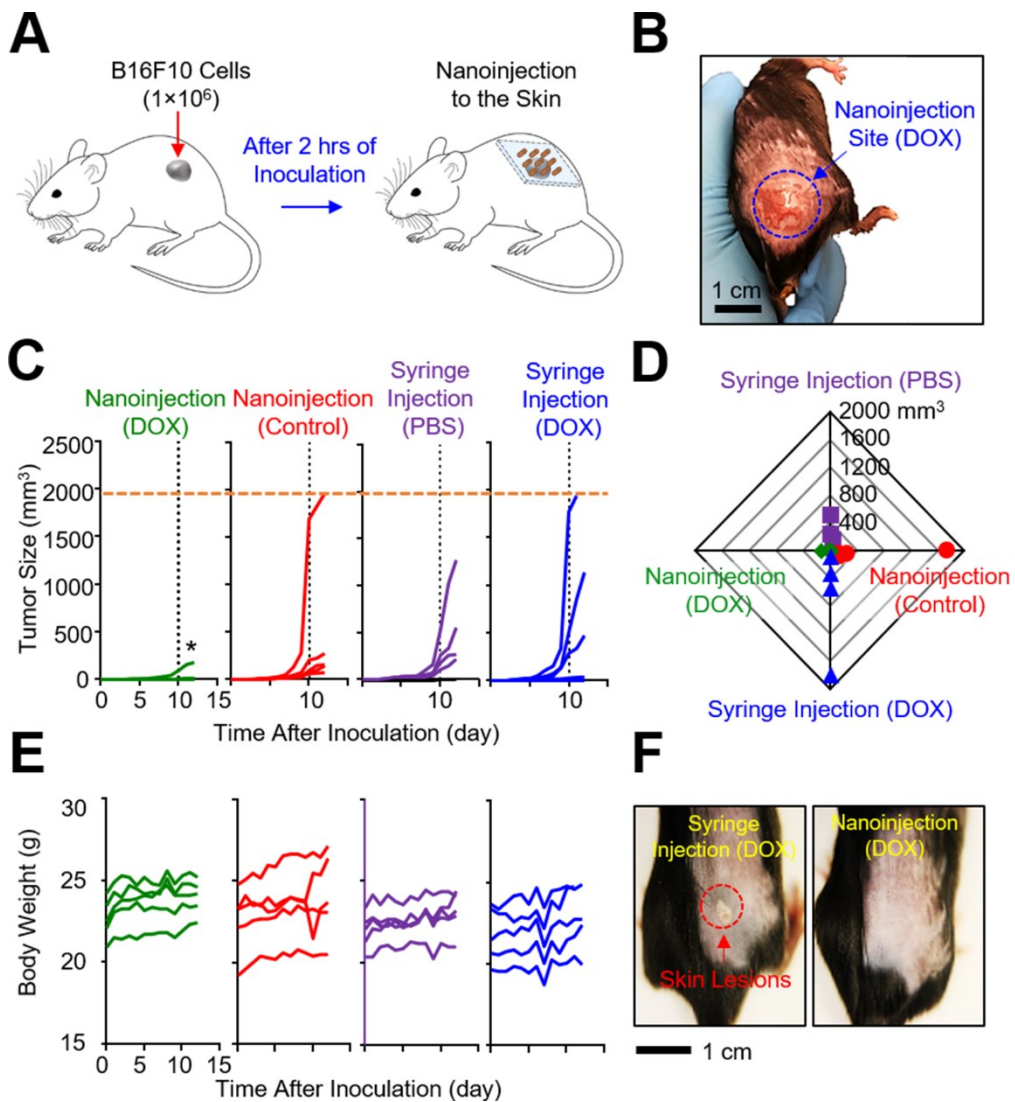


**Figure 3. Biocompatibility and controlled drug release.** (A) Real-time bioluminescence images on the epidermis (on top of the skin) and subcutaneous muscle (under the skin) of mice at 5 h following the implementation of the p-Si needles built on a medical-grade PVA (left column), industrial-grade PVA (middle column), and control PMA treatments (right column). (B) Results of MTT assay in the cytotoxicity tests of HDF cells incubated with a medical-grade PVA with (red bars) and without (blue bars) the p-Si needles, as well as an industrial-grade PVA (green bars). Error bars represent the standard deviation (SD) of three replicates. \*\*\*p<0.0001 compared to the medical-grade PVA with the p-Si needles using one-way analysis of variance (ANOVA). (C) Confocal microscopy image of the p-Si needles loaded with DOX. (D) Confocal microscopy image of the p-Si needles embedded inside a 2.8% (w/v) agarose gel (color index by penetration length). (E) Cumulative release of DOX obtained from the p-Si needles with varied surface porosities of 0%, 30%, 45% and 60% after 20 days of the immersion in PBS (pH 7.4) at 37.5 °C. \*p<0.05 compared to 0% surface porosity using ANOVA. (F) Release profiles obtained from the p-Si needles with covalently-linked DOX, compared to median lethal dose of DOX in mice (LD<sub>50</sub>, green dotted line). (G) Release profiles obtained from the p-Si needles with the surface porosity of ~45% using amide (red line), urea (blue line), and control physical (black line) bonds of DOX. \*\*p<0.01 and \*\*\*p<0.0001 compared to the control physical bond using ANOVA. (H) Cumulative release (%) of the covalently-linked (amide and urea bonds) DOX, compared to the control physically trapped DOX.



1  
2

3 **Figure 4. Unobtrusive topical delivery of the p-Si needles.** (A) Optical images of the p-Si  
4 needles with DyLight 800 fluorescent dyes on a PVA film, applied to the epidermis (left image),  
5 subcutaneous muscle (middle image), and cornea (right image) of mice. (B) IVIS images of the  
6 mice receiving the p-Si needles for 2 days following the implementations.



1   **Figure 5. Evaluations in a murine melanoma model in vivo.** (A) Schematic illustration of  
2 experimental protocols for in vivo studies in a murine melanoma model. (B) Representative image  
3 of the shaved skin of a mouse post-nanoinjection of DOX. (C) Measurement results of the tumor  
4 size for 12 days post-inoculation ( $n = 5$  per group). \* $p < 0.05$  compared to the control syringe  
5 injection (DOX) using ANOVA. (D) Radial shape graph of the tumor size at day 10 ( $n = 5$  per  
6 group). (E) Measurement results of the body weight for 12 days post-inoculation ( $n = 5$  per group).  
7 (F) Representative images highlighting the treated sites for 10 days post-injection. The red dotted  
8 circle denotes skin lesions.  
9  
10

## 1 Table of Contents

2 Bioresorbable, miniaturized porous silicon needles on a water-soluble patch for the management  
3 of melanoma skin cancer.

4

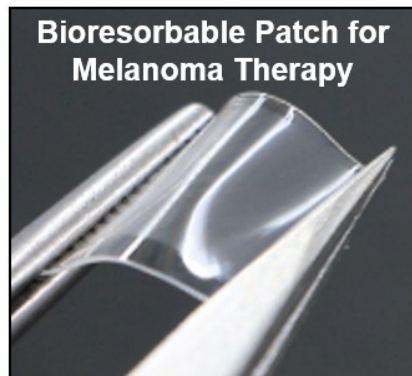
5

6

## ToC figure

7

8



# 1 Supporting Information

## 2 **3 Bioresorbable, miniaturized porous silicon needles on flexible** 4 **water-soluble backing for unobtrusive, sustained delivery of** 5 **chemotherapy**

6  
7 *Hyungjun Kim<sup>†,‡,§</sup>, Heungssoo Lee<sup>§,‡</sup>, Yale Jeon<sup>§</sup>, Woohyun Park<sup>¶</sup>, Yue Zhang<sup>¶</sup>, Bongjoong Kim<sup>¶</sup>,*  
8 *Hanmin Jang<sup>§</sup>, Baoxing Xu<sup>¶</sup>, Yoon Yeo<sup>†,\*</sup>, Dong Rip Kim<sup>§,\*</sup>, Chi Hwan Lee<sup>†,¶,‡,§,\*</sup>*

9  
10 <sup>†</sup>Weldon School of Biomedical Engineering, Purdue University, West Lafayette, IN 47907, USA.

11 <sup>‡</sup>Department of Industrial and Physical Pharmacy, Purdue University, West Lafayette, IN 47907,  
12 USA.

13 <sup>§</sup>School of Mechanical Engineering, Hanyang University, Seoul, South Korea.

14 <sup>¶</sup>School of Mechanical Engineering, Purdue University, West Lafayette, IN 47907, USA.

15 <sup>||</sup>Department of Mechanical and Aerospace Engineering, University of Virginia, Charlottesville,  
16 VA 22904, USA

17 <sup>¶</sup>School of Materials Engineering, Purdue University, West Lafayette, IN 47907, USA.

18 <sup>¶</sup>Department of Speech, Language, and Hearing Sciences, Purdue University, West Lafayette, IN  
19 47907, USA

20  
21 **Keywords:** *Melanoma Treatment, Topical Drug Delivery, Bioresorbable Silicon Nanomaterials,*  
22 *Sustained Drug Release*

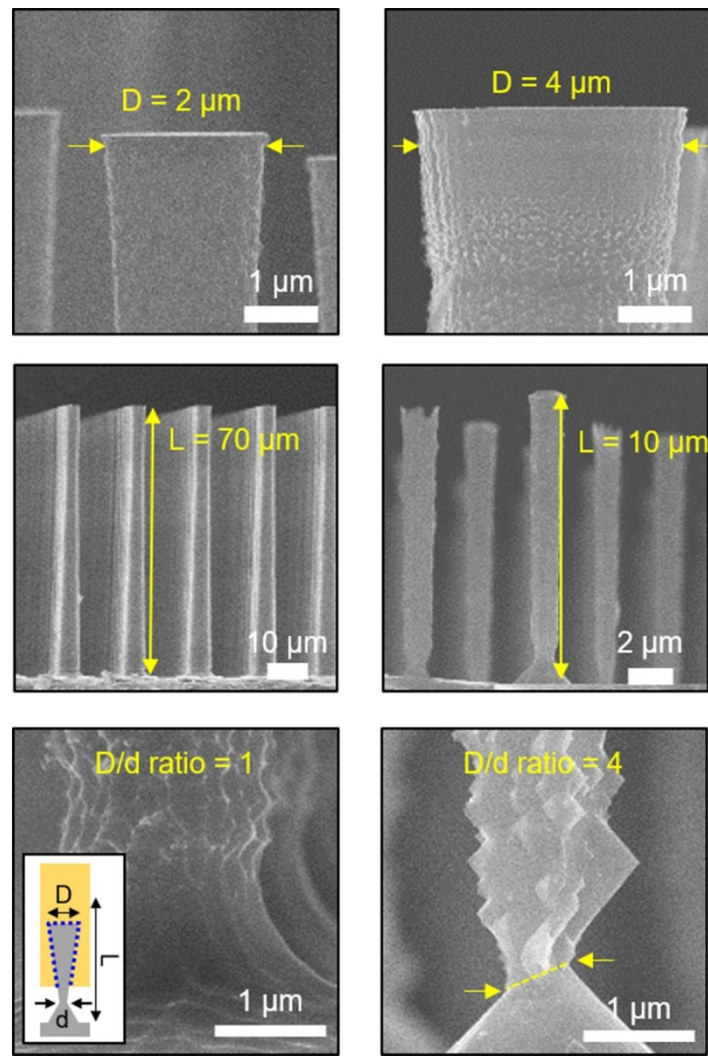
### 24 **Supplementary Movie Legends**

25 **Movie S1.** Visual observation (16 $\times$  speed) of a yellow-colored PVA immersed in a solution of  
26 PBS (pH 7.4) at 37.5 °C.

27  
28 **Movie S2.** Real-time demonstration of the automated peeling of the p-Si needles from the donor  
29 Si wafer

30  
31 **Movie S3.** Demonstration (26 $\times$  speed) of the nanoinjection of DOX to the shaved skin of a mouse  
32 after 2 h of subcutaneous inoculation with 1 $\times$ 10<sup>6</sup> B16F10 melanoma cells.

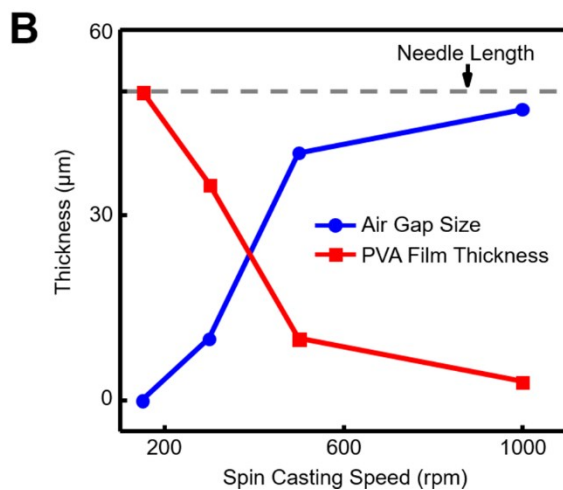
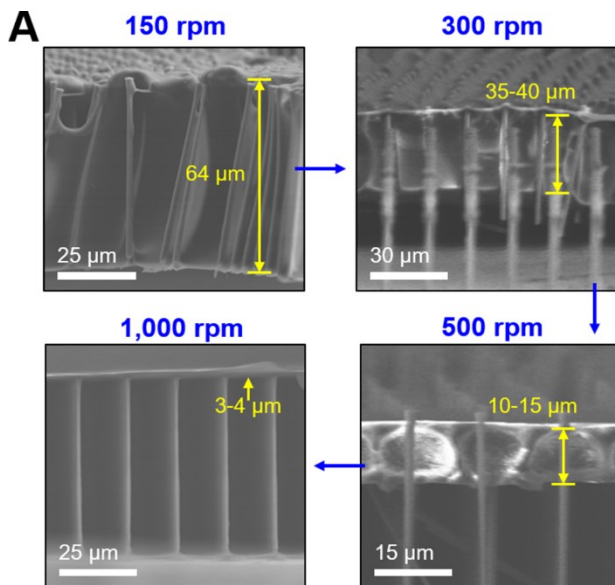
33  
34 **Movie S4.** Visual observation (2 $\times$  speed) of a mouse receiving an array (1 $\times$ 1 cm<sup>2</sup>) of the p-Si  
35 needles with covalently-linked (amide) DOX on the back side.



1  
2  
3  
4  
5  
6

**Figure S1.** SEM images of the p-Si needles fabricated on a donor Si wafer with varied geometries. The inset schematic image denotes the base diameter ( $D$ ) and undercut diameter ( $d$ ) of the p-Si needles.

1

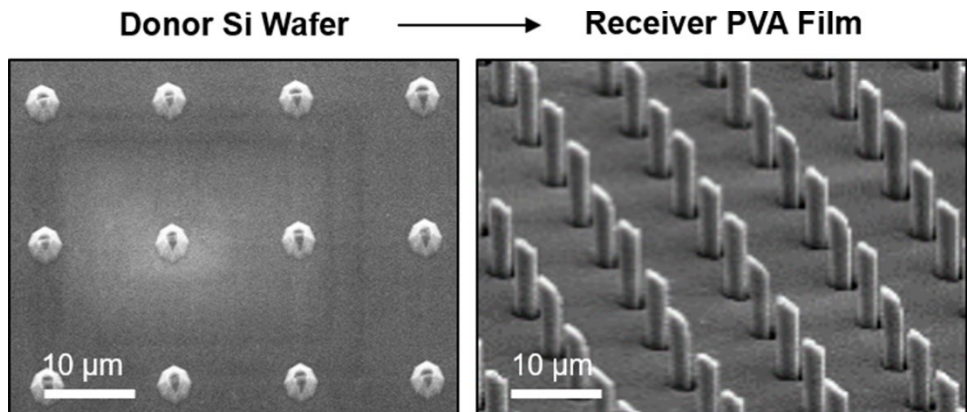


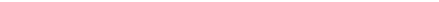
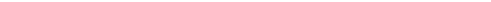
2

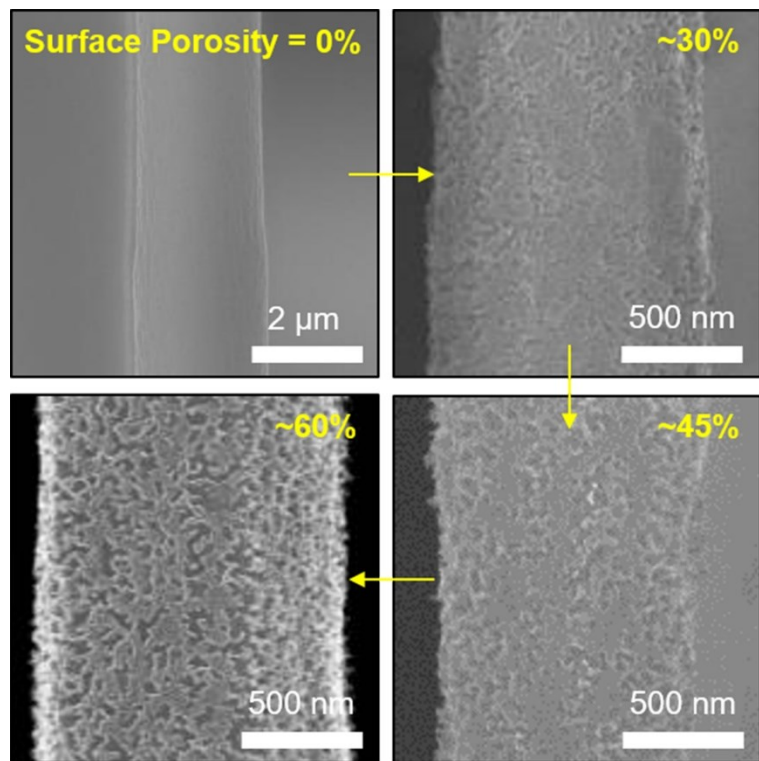
3

4

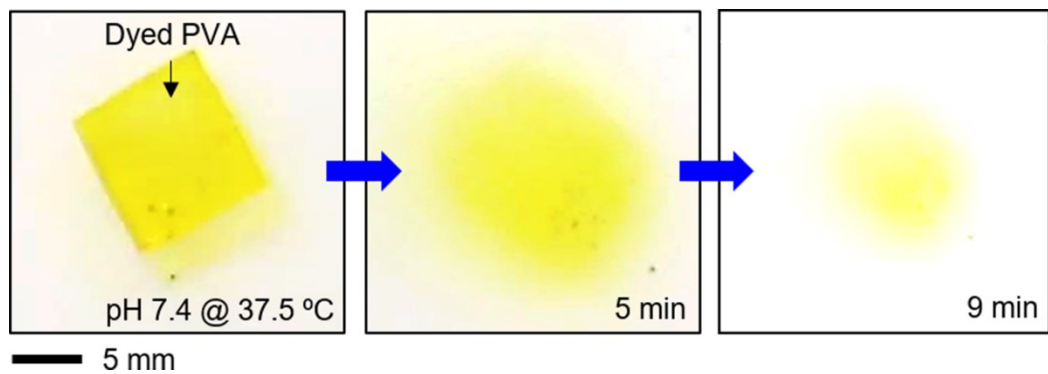
5 **Figure S2.** (A) SEM images of the PVA film coated on the p-Si needles at varied spin-casting  
6 speeds of 150, 300, 500, and 1,000 rpm from the left. (B) Plot of the measured thicknesses of the  
7 PVA film and air gap size as a function of spin casting speed ranging from 150 rpm to 1,000 rpm.



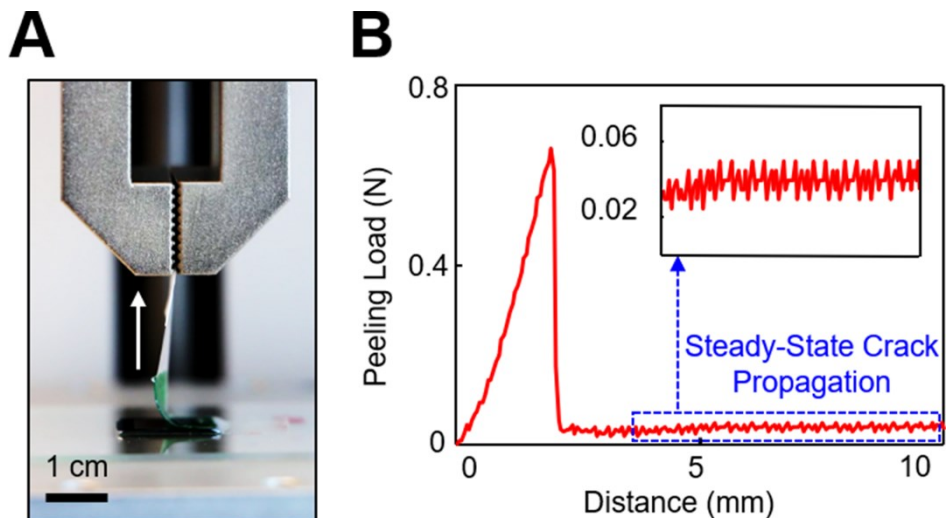
1   
 2   
 3 **Figure S3.** SEM images of a donor Si wafer (left image) and receiver PVA film (right image).



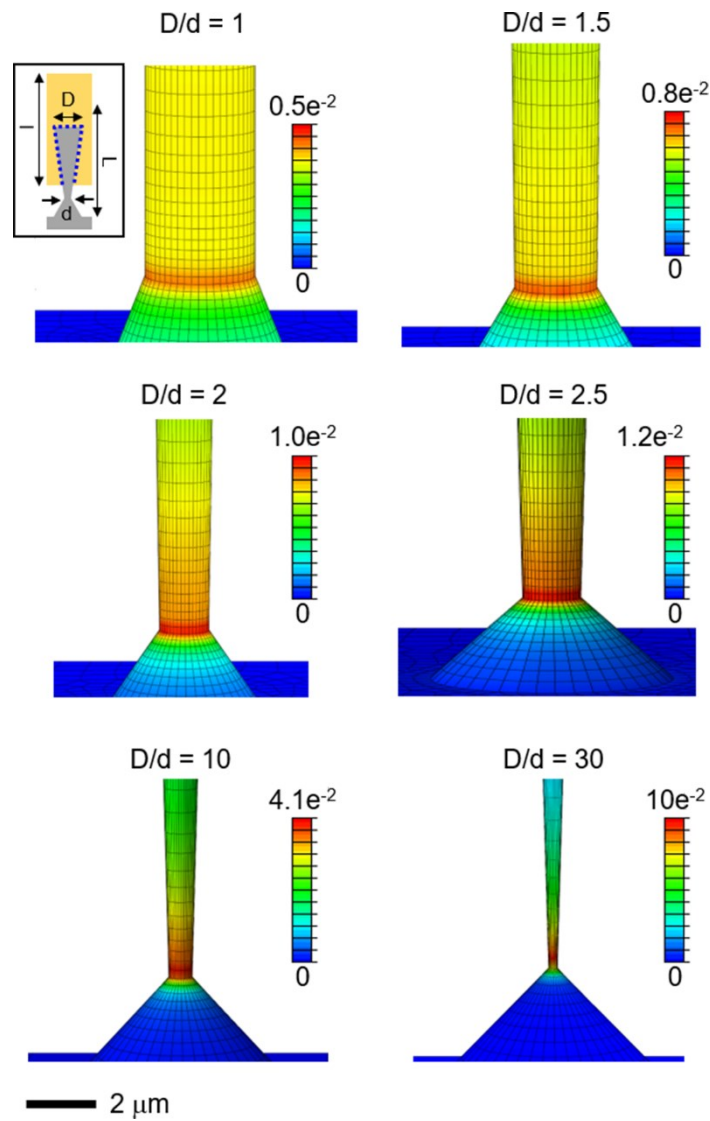
1  
2  
3 **Figure S4.** SEM images of the p-Si needles with varied surface porosities of 0%, 30%, 45%, and  
4 60%.



1  
2  
3 **Figure S5.** Time-dependent optical images of a yellow-colored PVA film immersed in a solution  
4 of PBS (pH 7.4) at 37.5 °C.



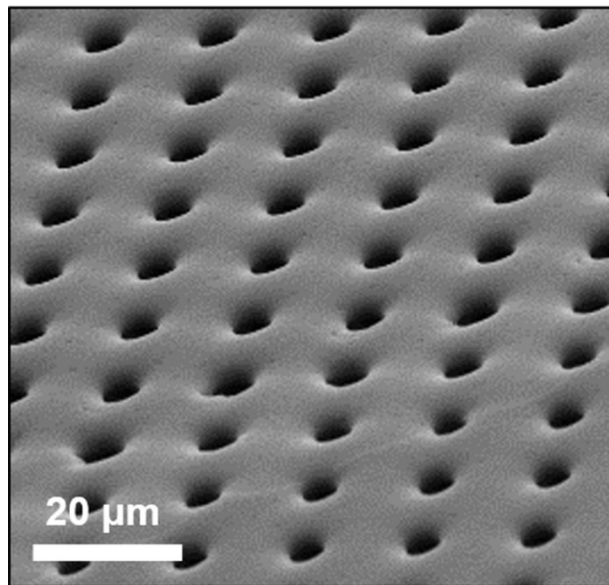
1  
2  
3  
4 **Figure S6.** (A) Optical image of an experimental setup for the automated peeling of the p-Si  
5 needles from the donor Si wafer. (B) Measurement results of the peeling load obtained from a unit  
6 specimen ( $1 \times 1 \text{ cm}^2$ ).



1  
2 **Figure S7.** FEA results displaying the distribution of principal strains along the p-Si nanoneedle  
3 with varied D/d ratios under constant mechanical peeling.  
4

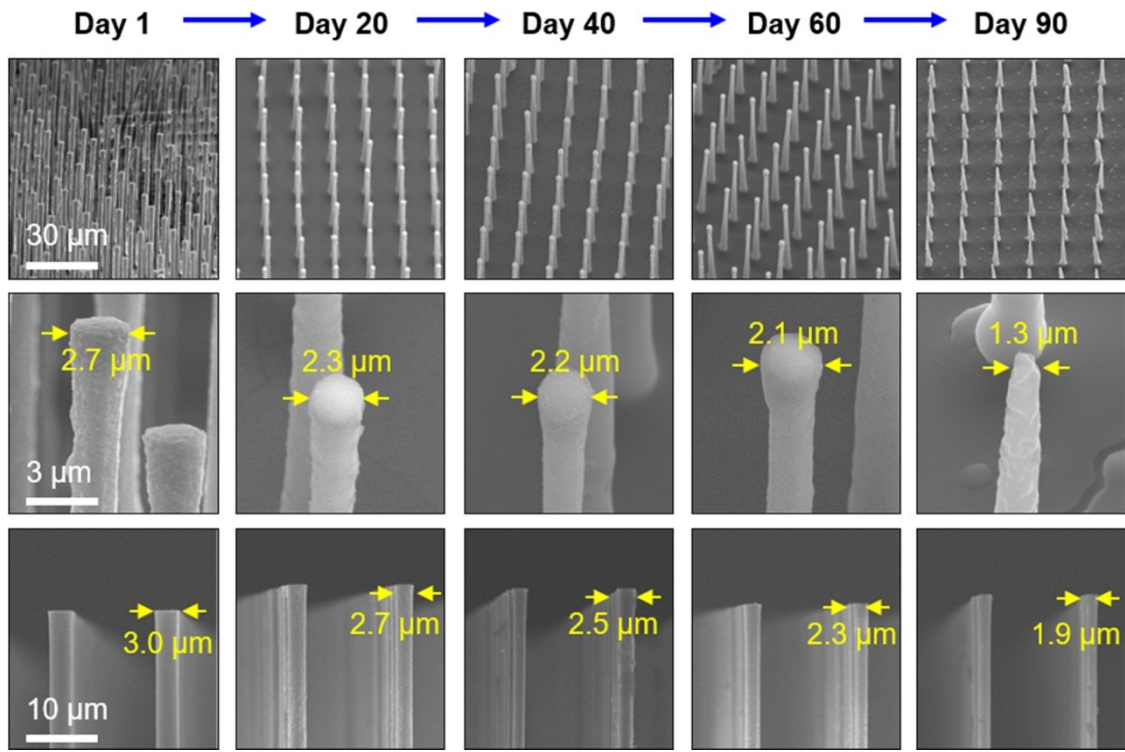
1  
2

## Receiver PVA Film

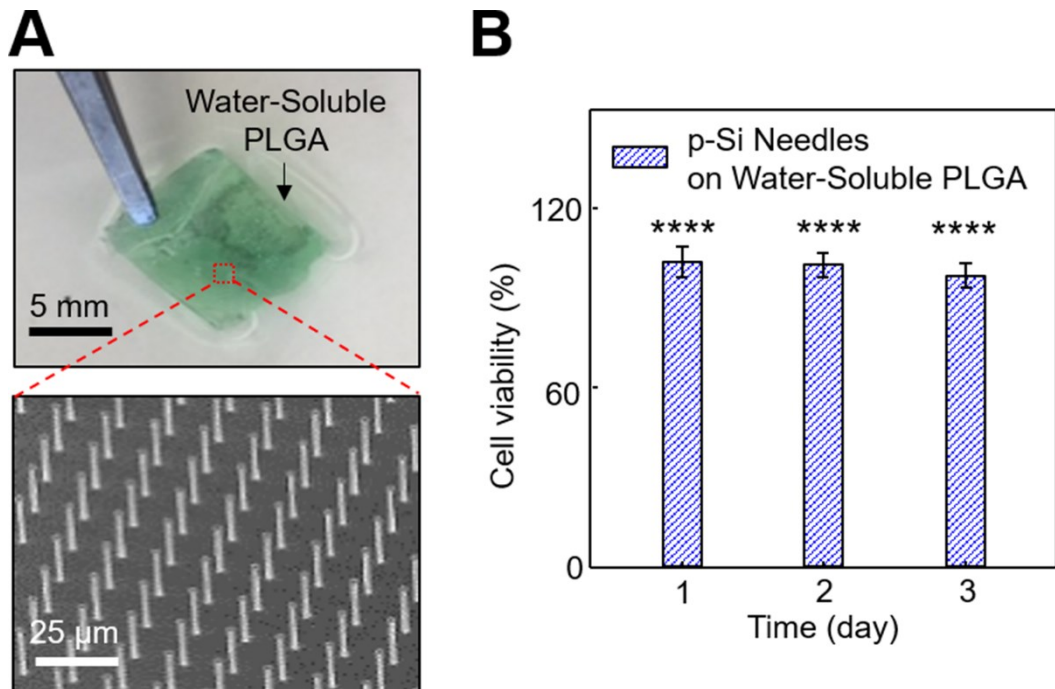


3  
4

5 **Figure S8.** Representative SEM image displaying the compressed marks leftover on the surface  
6 of a PVA film peeled out of optimal conditions.

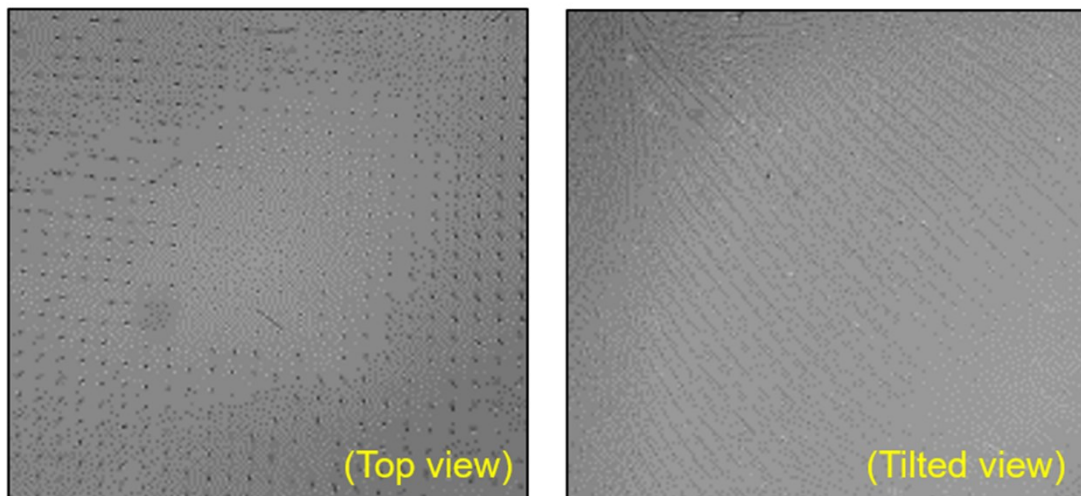


1  
2  
3  
4 **Figure S9.** SEM images of the p-Si needles immersed in 50 ml of PBS (pH 7.4) at 37.5 °C for 90  
5 days.



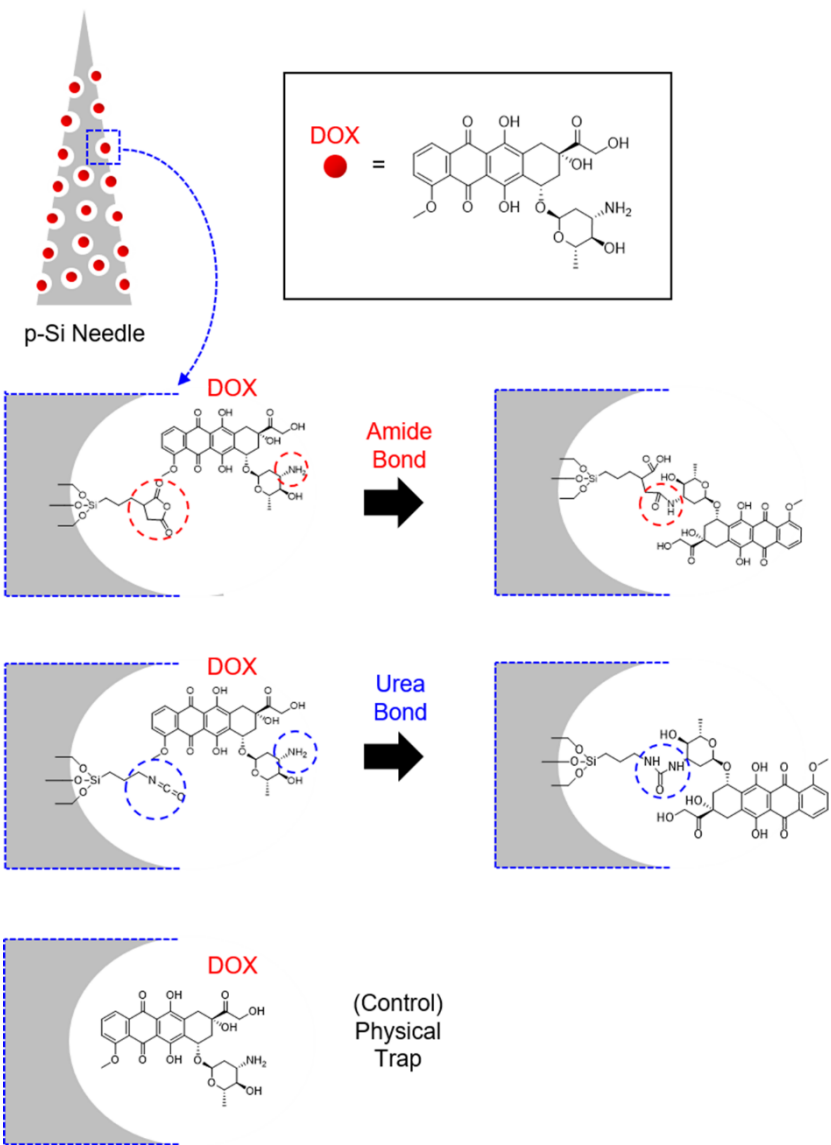
1  
2  
3  
4 **Figure S10.** (A) Photograph (top panel) and SEM (bottom panel) images of the p-Si needles built  
5 on a water-soluble PLGA film. (B) Corresponding results of MTT assay for the cytotoxicity test  
6 of HDF cells. Error bars represent the SD of the three replicates. \*\*\*p<0.0001 compared to the  
7 industrial-grade PVA with the p-Si needles using ANOVA.

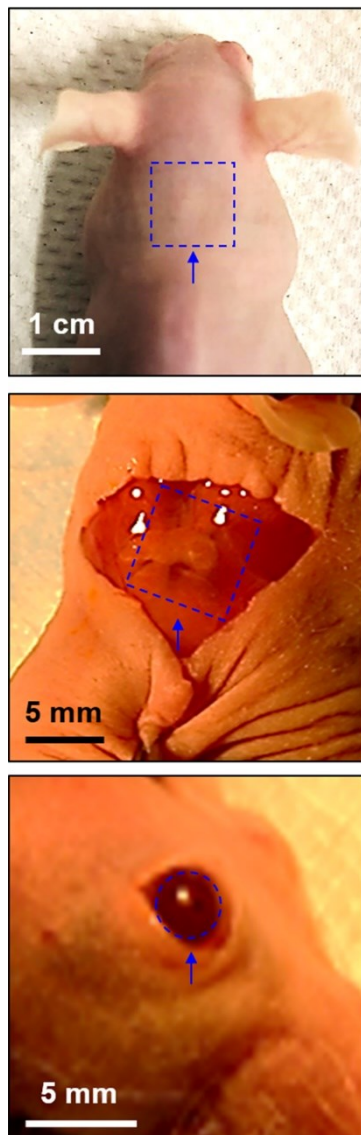
1  
2 **p-Si needles penetrated into an agarose gel**



5 **70 μm**

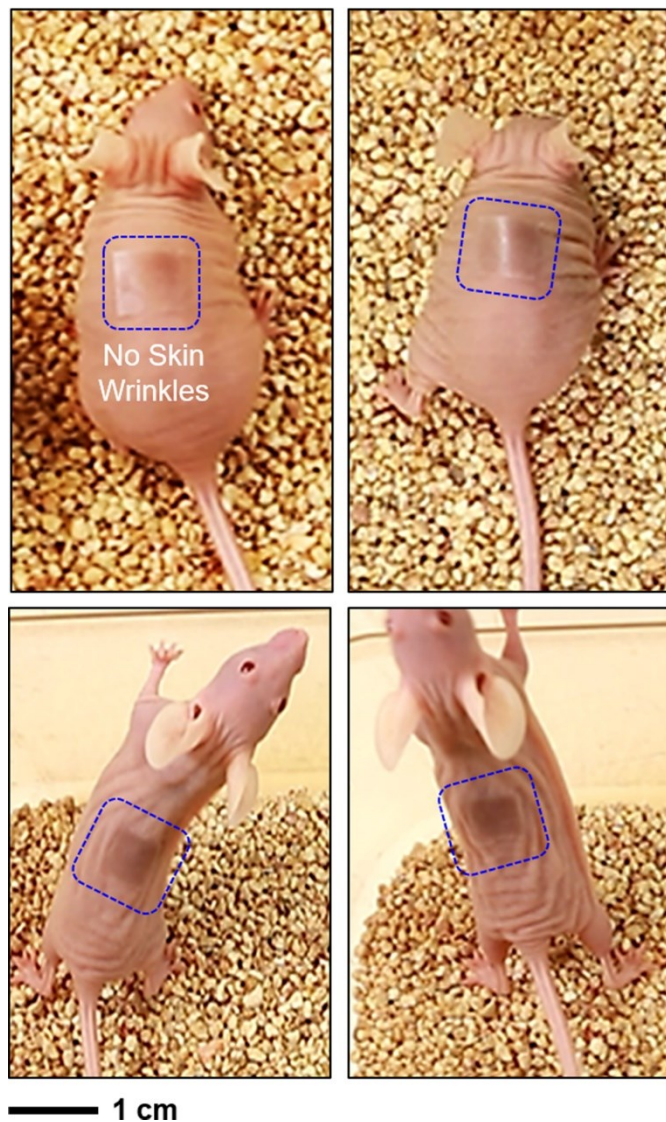
1  
2  
3  
4 **Figure S11.** Top-view (left image) and tilted-view (right image) microscope images of the p-Si  
5 needles penetrated into a 2.8% (w/v) agarose gel.





1  
2  
3  
4  
5

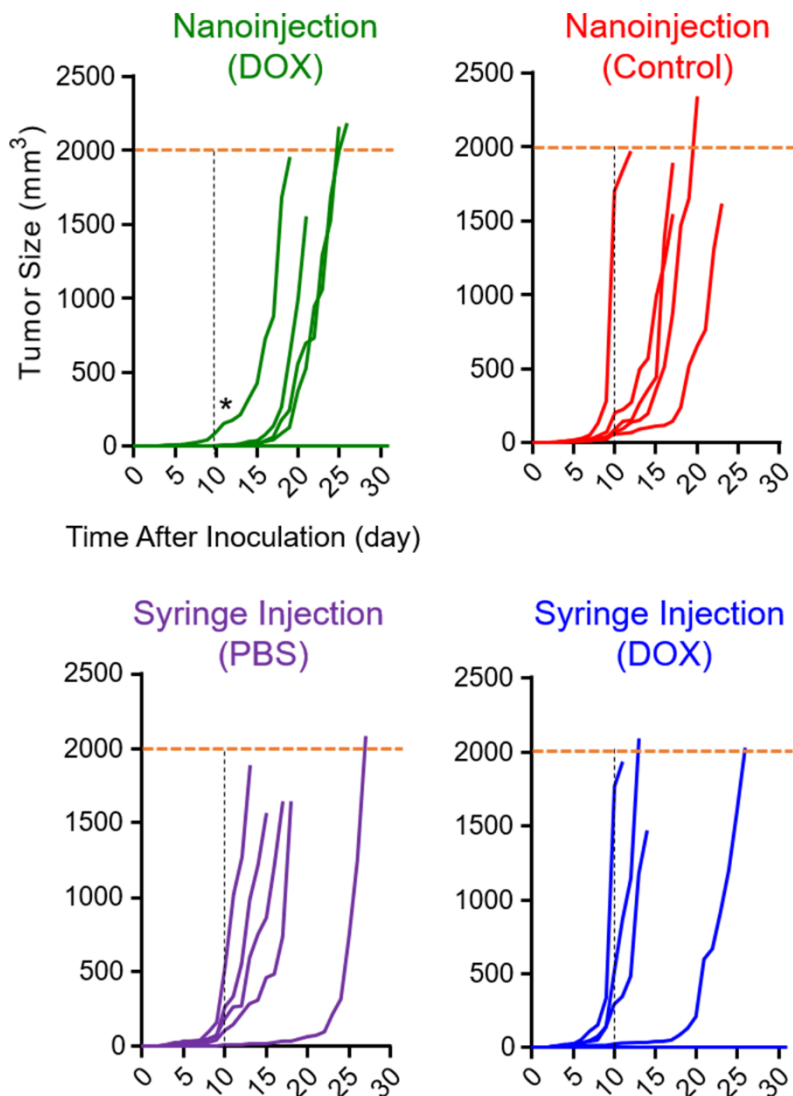
**Figure S13.** Enlarged optical images of the epidermis, subcutaneous muscle, and cornea of mice receiving the p-Si needles



1  
2

3 **Figure S14.** Optical images of a nude mouse worn with the control p-Si needles built on a PDMS  
4 film on the backsdie.

1



2

3

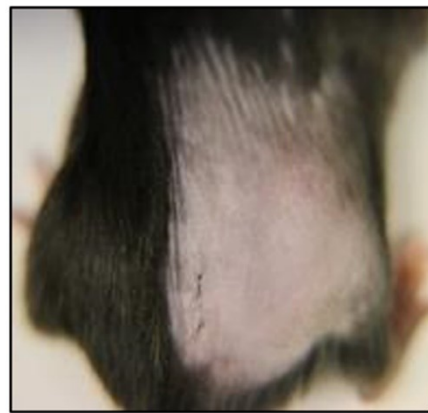
4 **Figure S15.** Measurement results of the tumor size ( $n = 5$  per group). The mice were humanely  
 5 sacrificed when the tumor size reached the endpoint of  $2,000 \text{ mm}^3$ . \* $p < 0.05$ , compared to the  
 6 control syringe injection (DOX) using ANOVA.

1

Nanoinjection (DOX)



Nanoinjection (Control)



Syringe Injection (PBS)



Syringe Injection (DOX)



2  
3  
4 **1 cm**

**Figure S16.** Enlarged optical images of the treated sites of the mice at 10 days post-injection